Kamliya Jawahar, H., Meloni, S., Camussi, R., & Azarpeyvand, M. (2021). Intermittent and stochastic characteristics of slat tones. *Physics of Fluids*, *33*(2), [025120 (2021)]. https://doi.org/10.1063/5.0033827

# Intermittent and stochastic characteristics of slat tones

Hasan Kamliya Jawahar,[1, a)] Stefano Meloni,[2, b)] Roberto Camussi,[3, c)] and Mahdi Azarpeyvand[4, d)]

[1)] *Research Associate, Department of Aerospace Engineering, University of Bristol, Bristol, BS8 1TR, United Kingdom.*

[2)] *PhD Student, Department of Engineering, University of Roma Tre, Rome 00146, RM, Italy.*

[3)] *Professor in Fluid Dynamics, Department of Engineering, University of Roma Tre, Rome 00146, RM, Italy.*

[4)] *Professor in Aerodynamics and Aeroacoustics, Department of Aerospace Engineering, University of Bristol, Bristol, BS8 1TR, United Kingdom.*

(Dated: 7 January 2021)

Experiments were conducted to assess the aeroacoustic characteristics of 30P30N three-element high-lift airfoil fitted with two different types of slat cove fillers at the aeroacoustic facility at the University of Bristol. The results are presented for the angle of attack $\alpha = 18°$ at a free-stream velocity of $U_\infty = 30$ m/s, which corresponds to a chord-based Reynolds number of $Re_c = 7 \times 10^5$. Simultaneous measurements of the unsteady surface pressure were carried out at several locations in the vicinity of slat cove and at the far-field location to gain a deeper understanding of the slat noise generation mechanism. The results were analyzed using a higher-order statistical approach to determine the nature of the broadband hump seen at low-frequency for the 30P30N high-lift airfoil observed in recent studies and also to further understand the tone generation mechanism within the slat cavity. Intermittent events induced by the resonant mechanism between the slat and its trailing edge were investigated in detail. A series of correlation and coherence analysis of the unsteady surface pressure measurements was carried out to identify and isolate the low-frequency hump. Wavelet analysis was performed to investigate the nature of the slat-wing resonant intermittent events in both time and frequency domains. Novel approaches, Dynamic Mode Decomposition and Multi-resolution Dynamic Mode Decomposition were applied to the wavelet coefficient moduli to determine the nature of the noise.

Keywords: 30P30N, High-lift airfoil, Slat noise, Slat cove filler, Aeroacoustics, Tones

[a)]Electronic mail: hasan.kj@bristol.ac.uk

[b)]Electronic mail: stefano.meloni@uniroma3.it

[c)]Electronic mail: roberto.camussi@uniroma3.it

[d)]Electronic mail: m.azarpeyvand@bristol.ac.uk

## I. INTRODUCTION

The rapid growth of the aircraft industry constantly demands for more efficient and quieter aircraft than the ones currently in service. The impact of noise generated by aircraft during take-off and landing has come under scrutiny over the past decades especially with the increasing popularity of air travel and expansion of airports. Although aircraft engine noise has been substantially reduced by the use of high bypass engines, the airframe noise remains a major contributor to aircraft noise. In order to reduce these prominent noise sources, several passive and active flow control methods[1,2] have been investigated in the past, including morphing structures[3–9], porous materials[10–12], surface treatments[13], and serrations[14–17]. High-lift devices, namely slats and flaps are one of the major contributors to airframe noise. Their noise generation mechanism is of both broadband and narrowband in nature. Studies on conventional slat and wing configurations have shown that they mainly comprise of broadband and tonal noise components. The emergence of discrete tones at mid-frequency range has been reported in multiple studies[18–33]. The number of these tonal peaks decrease with the angle of attack and their amplitude decreases with increasing slat gap and overlap[27]. However, their noise generation mechanism is yet to be fully understood.

Several successful studies[34–44] were carried out over the past two decades to reduce the characteristic noise arising from the slat. This was achieved by enclosing the recirculation region within the slat cavity. The characteristic tones from the slat arise as a result of the feedback loop between the vortex shedding emanating from the slat cusp and its impingement on the slat lower surface. In order to eliminate this tonal and broadband noise from the shear layer instability and impingement, the slat cavity was enclosed with a solid filler having an aerodynamic profile. Horne *et al.*[34], from NASA, in order to eliminate the unsteady recirculation region within the slat cove, tested a solid Slat Cove Filler (SCF) and revealed that it was effective in reducing broadband slat noise up to 4-5 dB. Streett *et al.*[35] further demonstrated that the noise reduction was sensitive to the angle of attack and SCF modification. Furthermore, the SCF modification showed a reduction of 3-5 dB over a wide spectrum. Imamura *et al.*[38] and Ura *et al.*[39], from JAXA, showed that noise reduction of up to 5 dB could be achieved with the use of slat cove fillers, both experimentally and computationally.

Previous studies[18–33] have indicated that the strong tonal peaks in the mid-frequency range ($St_s = 1 - 5$) are generated by the flow acoustic cavity feedback mechanism of slat cove shear

layer instabilities. Additionally, a possible quadratic interaction between the tonal peaks were observed[25–29].

In general, broadband humps observed at low-frequency range ($St_s < 1$) in previous studies were assumed to be part of the cavity feedback mechanism. However, in a recent study, Kamliya *et al.*[4] hypothesized that the first Rossiter mode is most likely to be concealed within the broadband hump $0.5 < St_s < 1$ and that the source of that broadband hump is not solely due to the Rossiter modes. The Rossiter modes arise as a result of flow-induced oscillations from the vortex shedding at the slat cusp and the resulting acoustic feedback mechanism portrays distinct narrowband peaks. Further higher-order spectral analysis of near field pressure fluctuations demonstrated strong self-interaction of the broadband hump ($0.5 < St_s < 1$), with no cross-interaction, confirming the varying nature of the broadband hump. Whereas the other narrowband peaks showed high levels of quadratic coupling and cross-interaction reaffirming mode interactions. Moreover, the results from the persistence spectrum of the surface pressure fluctuations indicated that the broadband hump ($0.5 < St_s < 1$) was not persistent over the time period like the other narrowband peaks, instead the energy of the broadband spectra was evenly distributed in time over the entire frequency range.

Although several studies[34–43] have reported the aerodynamic and aeroacoustic behavior of slat cove fillers, further fundamental physics of the noise generation mechanism of the slat and the noise suppression mechanism of the slat cove fillers are yet to be fully understood. It is well established from previous studies[18–33] that the source of the tonal peak is due to the Rossiter modes that arise from the interaction between the slat cusp and its trailing edge, however the nature and the source of the broadband hump at low-frequency is yet to be identified and documented[4]. The present study aims to use a highly instrumented high-lift airfoil to establish the nature and identify the source of the broadband hump in question. Complementing the previous works on slat cove filler by Kamliya *et al.*[4] this study presents improved unsteady pressure measurements at several locations within the slat cove region for three different configurations. In addition to the standard Fourier transform based analysis, this paper uses new approaches including wavelet analysis coupled with stochastic analysis to improve the understanding of this low-frequency broadband hump and the slat noise generation mechanism. Data were analyzed providing an exhaustive intermittency characterization including spectral quantities, cross-correlations, and continuous wavelet transform. Furthermore, Dynamic Mode Decomposition technique has also been used as a data-driven analysis tool applied to the wavelet coefficient moduli from various sensors within the slat cove region to extract meaningful

spatio-temporal patterns that dominate dynamic activity in the broadband hump and the slat tone. Multi-resolution Dynamic Mode Decomposition was used to identify the low-frequency pulsation of the broadband hump.

## II. EXPERIMENTAL SETUP

### A. Airfoil Setup

A three-element 30P30N high-lift airfoil with a retracted chord length of $c = 0.35$ m and a span length of $l = 0.53$ m was manufactured in aluminum using a computer-aided numerically controlled machine. The geometrical parameters of the high-lift airfoil are detailed in Table. I and depicted in the schematic in Fig. 1. Furthermore, brackets between the main-element and slat were not used in the spanwise direction to retain two-dimensionality within the slat cove region. Instead, steel clamps were used on the side of the airfoil after the side plates to attach the three-elements. A zig-zag turbulator tape with a thickness of $h_t = 0.5$ mm and a width of $w_t = 6$ mm with a turbulator angle of 70° was used at $x/c = -0.055$ on the pressure side of the slat surface upstream of the slat cusp to trip the flow and to induce turbulent shear layer[21]. The aforementioned 30P30N high-lift airfoil model was thoroughly studied at different test conditions and its aerodynamic and aeroacoustic performance was validated[3,4] against the existing benchmark studies[23].

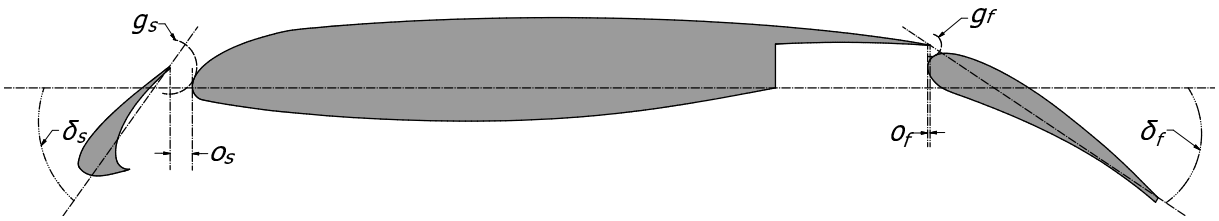


**FIG. 1:** Geometric parameters of the 30P30N three-element high-lift airfoil.

#### *1. Slat cove-filler design*

In the present study, Half slat cove filler (H-SCF) and Slat cove filler (SCF) configurations were tested for the purpose of slat noise reduction. The H-SCF configuration was observed to exhibit favorable aerodynamic and noise reduction properties in computational studies by Tao and Sun[43]

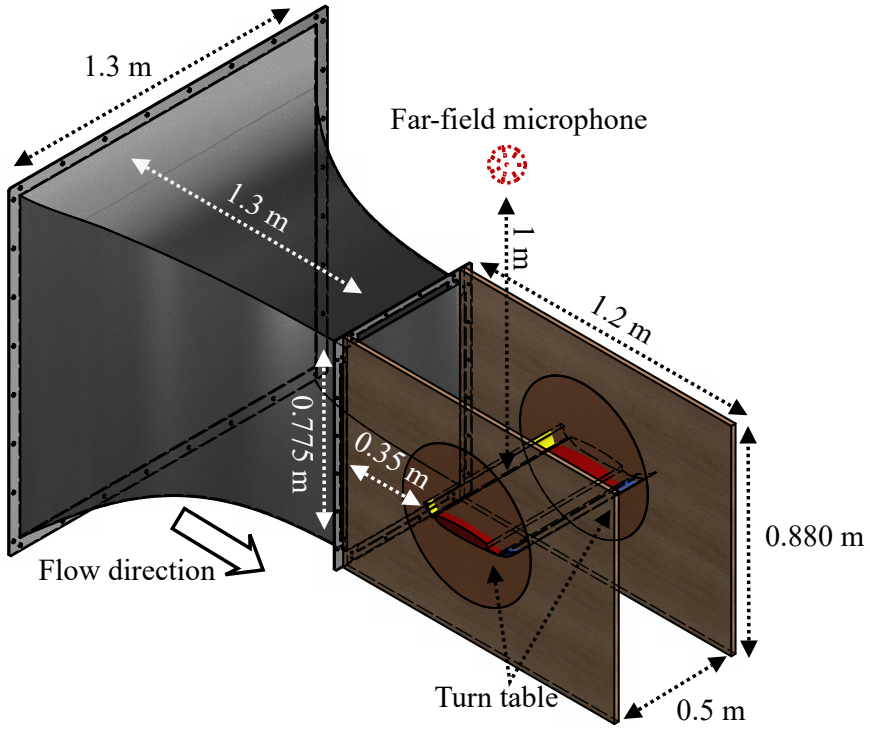


**FIG. 2:** Schematic of the experimental set-up.

**TABLE I:** Geometrical parameters in percentage of stowed airfoil chord, $c = 0.35$ m.

| | | |
|---|---|---|
| Slat chord | $c_s$ | $0.15c$ |
| Main-element chord | $c_{me}$ | $0.83c$ |
| Flap chord | $c_f$ | $0.3c$ |
| Slat deflection angle | $\delta_s$ | $30°$ |
| Flap deflection angle | $\delta_f$ | $30°$ |
| Slat gap | $g_s$ | $2.95\%$ |
| Flap gap | $g_f$ | $1.27\%$ |
| Slat overhang | $o_s$ | $-2.5\%$ |
| Flap overhang | $o_f$ | $0.25\%$ |

and experimental studies by Kamliya *et al.*[4]. The SCF configuration tested in this study was similar to that introduced by Imamura *et al.*[38,39]. The SCF profile was designed using the slat cusp shear layer trajectory possessing high turbulent kinetic energy at the angle of attack $\alpha = 8°$ extracted from RANS steady-state simulation of the Baseline configuration. Both the slat cove-fillers were

manufactured using 3D printing technology, in four different sections such that they could be slid along the span of the slat cove. It should be noted that although the SCF is designed for a free-stream angle of attack of $\alpha = 8°$, the aerodynamic characteristics of the high-lift device remain unaffected over a wider range of angles of attack, as shown by Kamliya *et al.*[4].

## B. Wind-Tunnel and installation setup

Aeroacoustic measurements for the 30P30N high-lift airfoil were carried out at the University of Bristol Aeroacoustic Facility[45]. The closed-circuit open-jet anechoic wind tunnel has a nozzle exit of 0.5 m × 0.775 m with a contraction ratio of 8.4:1. The wind tunnel is capable of velocities up to 40 m/s with turbulence levels as low as 0.25%[45]. The flow turbulence intensity (TI) was calculated using $u'_{rms}/U_{mean}$, where $u'_{rms}$ is the root-mean-square of the velocity fluctuations and $U_{mean}$ is the mean velocity. The effect of the large-scale facility unsteadiness from the turbulence intensity measurements was eliminated by applying a high-pass filter to the velocity fluctuations at $f = U_\infty/2L_{TS}$, where $L_{TS}$ is the largest test section dimension. A schematic of the airfoil installed in the wind tunnel is shown in Fig. 2. The airfoil was placed at a distance of $1c$ from the nozzle exit (see Fig. 2). The tests were carried out at the geometric angle of attack $\alpha = 18°$ for a free-stream velocity of $U_\infty = 30$ m/s, which corresponds to a chord-based Reynolds number of $Re_c = 7.0 \times 10^5$. It is important to note that the high-lift airfoils cause high-flow deflection and circulation region resulting in a difference of about 8.5° between the corrected and geometric angles of attack for high-lift airfoils in an open-jet configuration, as previously shown in other studies[4,46].

### *1. Acoustic measurements and instrumentation*

Several FG-3329-P07 pressure transducers from Knowles Electronics were installed on the main-element of the wing to measure the unsteady surface pressure around the slat region on the main-element (FG1-FG5, see Table. II). This pressure transducer was selected for the measurement of the near-field pressure as it was proven successful in the previous experiments carried out by Garcia and Hynes[47] on a NACA 0012 airfoil. The transducer placement on the main-element was based on the previous studies by Murayama *et al.*[23]. The transducer has a diameter of 2.5 mm and a height of 2.5 mm with a sensing area of 0.8 mm. Additionally, remote sensing microphone probes connected

to the pressure tap brass tube using a plastic tubing with an inner and outer diameter of 0.8 mm and 4 mm were employed to measure the unsteady surface pressure fluctuations on the slat and at various streamwise locations on the main-element (see Fig. 4 and Table. II)[48]. The remote sensors were made using Panasonic WM-61A microphones attached to 1.6 mm diameter brass tubes with 0.4 mm pinholes (see Fig. 3). In order to eliminate the spurious tones related to the standing waves in the flexible tubing, an acoustic termination tube of 2 m (determined from a parametric study) was used for each port (see Fig. 3). The far-field noise was measured using a Panasonic WM-61A microphone placed at an angle of 90° at a distance of 1 m away from the slat trailing edge. The near- and far-field microphones were calibrated using a G.R.A.S. 40PL microphone that is factory calibrated with a known manufacturer sensitivity[49].

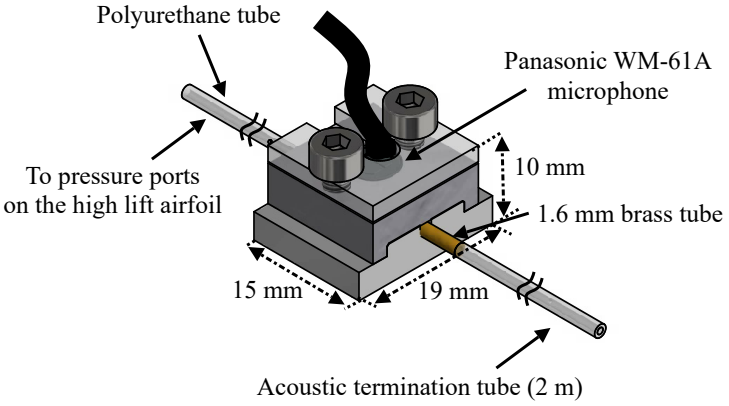


**FIG. 3:** Schematic of the remote sensor configuration.

A beamforming study using an array of 63 free-field microphones was carried out to evaluate the airfoil and side-plate junction noise. The junction noise showed an insignificant contribution to the slat frequencies ($> 3600$ Hz ($St_s \approx 6.2$)) that are of interest in the study. In contrast, the beamforming revealed that the primary noise source was clustered at the slat cove and well distributed over the span of the wing. Furthermore, results obtained from an individual far-field microphone followed a trend similar to that of the beamforming whilst accurately capturing the characteristic tonal peaks and broadband hump from the slat. Previous studies[4,29] have also established that individual far-field microphones were sufficient for the measurement of the dominant characteristic features of the slat noise.

National Instruments PXIe-4499 modules inserted in a National Instruments PXIe-1062Q chassis were used for data acquisition. The data were simultaneously collected for 120 seconds at a sampling

frequency of $f_s = 2^{15}$ Hz for all the near- and far-field microphones. The power spectrum results were obtained using the power spectral density (PSD) of the pressure signals with the Hanning window and were further averaged 220 times to yield a frequency resolution of $\Delta f = 2$ Hz. The statistics of the pressure fluctuation were evaluated using the following equation to obtain the Sound Pressure Level (SPL):

$$SPL = 20 \log_{10}\left(\frac{p_{rms}}{p_{ref}}\right), \tag{1}$$

where $p_{rms}$ is the root-mean-square of the acoustic pressure and $p_{ref} = 20\mu Pa$ is the reference pressure. The SPL and other results are presented in terms of Strouhal number ($St_s$), as defined as

$$St_s = \frac{f c_s}{U_\infty}, \tag{2}$$

where $c_s$ is the slat chord and $U_\infty$ is the free-stream velocity. The results of the unsteady surface pressure auto-spectra are presented in Fig. 6 for all the remote sensors (see Table II) and the tested slat configurations.

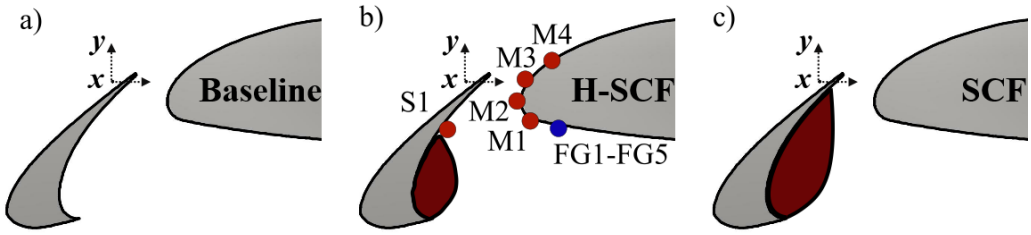


**FIG. 4:** Location of the unsteady pressure measurement probes (a) Baseline, (b) Half slat cove filler (H-SCF) and (c) Slat cove filler (SCF).

**TABLE II:** Streamwise and spanwise unsteady pressure measurement location on the 30P30N three-element high-lift airfoil.

| No. | $x$ (mm) | $y$ (mm) | $z$ (mm) |
|---|---|---|---|
| S1 | -6.918 | -11.622 | 265 |
| M1 | 17.347 | -10.019 | 265 |
| M2 | 15.126 | -5.839 | 265 |
| M3 | 17.622 | 0 | 265 |
| M4 | 23.520 | 5.485 | 265 |
| FG1 | 22.414 | -11.356 | 277 |
| FG2 | 22.414 | -11.356 | 280.6 |
| FG3 | 22.414 | -11.356 | 288.4 |
| FG4 | 22.414 | -11.356 | 301.4 |
| FG5 | 22.414 | -11.356 | 319.6 |

## III. DYNAMIC MODE DECOMPOSITION

A brief summary of the Dynamic Mode Decomposition (DMD) technique[50–53] employed in the current study is presented here. The *exact* DMD[52,53] method based on the following equations were applied on the wavelet coefficient moduli to understand the dynamic characteristic of the local oscillating features of the surface pressure measurement. As described by Kutz *et al.*[50], the data used for DMD involves two parameters, the number of spatial measurements per time snapshot ($n$), and the number of snapshots taken in time ($m$). In the present study, at first, the wavelet coefficient moduli ($|W_x|$) for a wide range of Strouhal numbers ($St_s = 0.2-8$) were calculated using the continuous wavelet transform detailed in Sec. IV C 2. The calculated wavelet coefficient moduli vary in intensity over time depending on the fluctuations of the pressure signal. The snapshot matrix $\boldsymbol{x_k}$, of dimension $n_x \times n_y$ is then generated, with $n_x = 4$ remote sensor locations (M1-M4, see Fig. 4) and $n_y = 171$ as the Strouhal numbers of interest, distributed between $St_s = 0.5 - 7$. The snapshot matrix ($\boldsymbol{x_k}$) is reshaped into a $n-$dimensional column vector ($n_x n_y \times 1$) with 684

rows. The data were collected at regularly spaced time intervals ($\Delta t$), given by:

$$t_{k+1} = t_k + \Delta t, \tag{3}$$

where the data snapshots are collected at $t_k$ from $k = 1, 2, ..., m$, for a total of $m$ measurement times. The data snapshots are arranged into two $n \times (m-1)$ matrices:

$$\boldsymbol{X} = [\boldsymbol{x_1}, \boldsymbol{x_2}, ....\boldsymbol{x_{m-1}}], \tag{4}$$

$$\boldsymbol{X'} = [\boldsymbol{x_2}, \boldsymbol{x_3}, ....\boldsymbol{x_m}]. \tag{5}$$

As can be seen from Eq. 4 and Eq. 5 the columns of $\boldsymbol{X'}$ are shifted one $\Delta t$ from those in $\boldsymbol{X}$. The $\boldsymbol{X}$ and $\boldsymbol{X'}$ can be written as,

$$\boldsymbol{X'} = \boldsymbol{A}\boldsymbol{X}, \tag{6}$$

where $\boldsymbol{A}$ is a best fit linear operator that can be described as a high-dimensional linear regression of the nonlinear dynamics that relate $\boldsymbol{X}$ to $\boldsymbol{X'}$[52]. The DMD of the data matrix pair ($\boldsymbol{X}$ and $\boldsymbol{X'}$) is given by the eigendecomposition of $\boldsymbol{A}$. The present snapshot $\boldsymbol{X}$ could be related to the future snapshot $\boldsymbol{X'}$ using the operator $\boldsymbol{A}$. This approach aims to solve the nonlinear dynamical system using the approximated optimal linear dynamics.

An approximation of $\boldsymbol{A}$ can be achieved using Single Value Decomposition (SVD) of the data matrix $\boldsymbol{X}$,

$$\boldsymbol{X} \approx \boldsymbol{U}\boldsymbol{\Sigma}\boldsymbol{V^*}, \tag{7}$$

where $*$ denotes the conjugate transpose, $\boldsymbol{U} \in \mathbb{C}^{n\times r}$, $\boldsymbol{\Sigma} \in \mathbb{C}^{r\times r}$, $\boldsymbol{V} \in \mathbb{C}^{m\times r}$. Here $r \leq m$ denotes either the exact or approximate rank of the reduced SVD approximation to $\boldsymbol{X}$. The left singular vectors $\boldsymbol{U}$ are proper orthogonal density (POD) modes. The columns of $\boldsymbol{U}$ are orthonormal, so $\boldsymbol{U^*U} = \boldsymbol{I}$; and similarly, $\boldsymbol{V^*V} = \boldsymbol{I}$[50,51].

According to Eq. 6, the full matrix $\boldsymbol{A}$ can be obtained by computing the pseudo-inverse of $\boldsymbol{X}$:

$$\boldsymbol{A} = \boldsymbol{X}\boldsymbol{U}\boldsymbol{\Sigma^{-1}}\boldsymbol{V^*}. \tag{8}$$

To obtain the leading $r$ eigenvalues and eigenvectors of $\boldsymbol{A}$, $\boldsymbol{A}$ could be projected onto the POD modes $\boldsymbol{U}$. By replacing equations (7) and (8) in (6), we obtain

$$\tilde{\boldsymbol{A}} = \boldsymbol{U}^* \boldsymbol{A} \boldsymbol{U} = \boldsymbol{U}^* \boldsymbol{X'} \boldsymbol{V} \boldsymbol{\Sigma}^{-1}. \tag{9}$$

Thus, the eigendecomposition of the matrix $\tilde{\boldsymbol{A}}$ can be computed by,

$$\tilde{\boldsymbol{A}} \boldsymbol{W} = \boldsymbol{W} \boldsymbol{\lambda}, \tag{10}$$

where $\boldsymbol{W}$ is the matrix with the eigenvectors and $\boldsymbol{\lambda}$ is containing the corresponding eigenvalues $\lambda_k$, respectively. Each non-zero eigenvalue $\lambda_k$ is a DMD eigenvalue. Then, the exact DMD modes $\boldsymbol{\Phi}$ are given by,

$$\boldsymbol{\Phi} = \boldsymbol{X'} \boldsymbol{V} \boldsymbol{\Sigma}^{-1} \boldsymbol{W}. \tag{11}$$

The approximate solution at all future times, $x_{DMD}(t))$, is given by,

$$\boldsymbol{x}_{DMD}(t) \approx \sum_{k=1}^{m} b_k \phi_k exp(\omega_k t) = \boldsymbol{\Phi} exp(\boldsymbol{\Omega} t) \boldsymbol{b}, \tag{12}$$

where $\boldsymbol{b}$ is vector of the coefficient $b_k$ is the initial amplitude of each mode, $\boldsymbol{\Phi}$ is the matrix whose columns are the eigenvectors $\phi_k$, $\boldsymbol{\Omega} = diag(\omega)$ is a diagonal matrix whose entries are the eigenvalues $\omega_k$, and $\omega_k = ln(\lambda_k)/\Delta t$.

### A. Multi-resolution DMD

In the present study, a new approach called multi-resolution Dynamic Mode Decomposition (mrDMD)[50] is explored to capture the frequency modulation by applying it on the wavelet coefficient moduli on a single remote sensor. This technique is based on a recursive approach to remove the low-frequency or slowly moving features from a snapshot series. The calculated wavelet coefficient moduli from the remote sensor signals were considered as a series of snapshots $m$. These $m$ snapshots contain a series with low- and high-frequency signatures.

Kutz *et al.*[50] have mathematically shown that the mrDMD separates the DMD approximate

solution (Eq. 12) at the first level as follows:

$$\boldsymbol{x}_{mrDMD}(t) = \sum_{k=1}^{m} b_k \boldsymbol{\phi}_k^{(1)} exp(\omega_k t) = \underbrace{\sum_{k=1}^{m_1} b_k \boldsymbol{\phi}_k^{(1)} exp(\omega_k t)}_{\text{slow modes}} + \underbrace{\sum_{k=m_1+1}^{m} b_k \boldsymbol{\phi}_k^{(1)} exp(\omega_k t)}_{\text{fast modes}}, \tag{13}$$

where $\boldsymbol{\phi}_k^{(1)}$ are the DMD modes evaluated from the full $m$ snapshots. We identify the slow modes with the first summation on the right side, whereas the second one defines the fast modes. Once again, the process is iteratively repeated, removing the slow modes at each step. The algorithm stops when the desired decomposition level is achieved, obtaining at the end a series of the matrix with modes at different frequencies. The final DMD approximation reads as:

$$\boldsymbol{x}_{mrDMD}(t) = \sum_{k=1}^{m_1} b_k^{(1)} \boldsymbol{\phi}_k^{(1)} exp(\omega_k^{(1)} t) + \sum_{k=1}^{m_2} b_k^{(2)} \boldsymbol{\phi}_k^{(2)} exp(\omega_k^{(2)} t) + \sum_{k=1}^{m_3} b_k^{(3)} \boldsymbol{\phi}_k^{(3)} exp(\omega_k^{(3)} t) + ....., \tag{14}$$

To summarize, $\boldsymbol{\phi}_k^{(i)}$ and $\omega_k^{(i)}$ are the DMD modes and DMD eigenvalues obtained at $i^{th}$ level of decomposition, the $b_k^{(i)}$ are the initial projections of the data onto the time interval of interest and $m_k$ is the number of slow modes retained at each level. Similarly, long, medium and short term trends in data are identified through successive levels containing faster modes. For detailed information on this method, the readers are referred to Kutz *et al.*[50].

## IV. RESULTS AND DISCUSSION

Aerodynamic characteristics of the 30P30N three-element high-lift airfoil tested at the University of Bristol with suggested slat modifications (H-SCF and SCF) have been well documented in a previous study by Kamliya *et al.*[4]. It has been established that the aerodynamic characteristics of the three-element high-lift airfoil were not affected by the slat modifications. The observations from the current experimental campaign will be presented in the following order. Firstly, the far-field acoustic characteristics of the tested slat configurations are presented. Subsequently, single and two-point spectral analysis of the near-field unsteady pressure measurements are analyzed in detail at various streamwise locations. Thorough wavelet analysis for various remote sensors is carried out and time-frequency analysis is performed using statistical mechanics. Finally, the dynamic characteristics of the time-frequency behavior of the pressure fluctuations are presented and analyzed.

### A. Far-field noise

The far-field noise levels for the 30P30N three-element high-lift airfoil with various slat cove filler configurations were measured using a single Panasonic WM-61A microphone away from the slat trailing edge at an angle of 90° and at a distance of 1 m. The far-field pressure fluctuations were analyzed in the frequency domain using SPL through Eq. 1. The SPL spectra for all the tested configurations are reported in Fig. 5. Evidently, the persistence of the tonal peaks close to $St_s = 1.6$ and $St_s = 3.2$ demonstrated the characteristic behavior of the slat noise. The SPL spectra for the surface mounted pressure sensors at FG1 are presented in Fig. 5(b) to show the general trend of the near-field pressure characteristics over a wide range of frequencies of up to $f = 10$ kHz ($St_s = 17.5$). It is apparent that the high-frequency dissipation within the tiny tubes of the remote sensors yields accuracy only over a narrow frequency range. In the current experimental setup, the remote sensors are accurate and valid only up to $f = 6$ kHz ($St_s = 10$). Accordingly, it is evident from Fig. 5(b) that a frequency of about $f = 6$ kHz ($St_s = 10$) was sufficient to capture the dominant characteristics of slat noise.

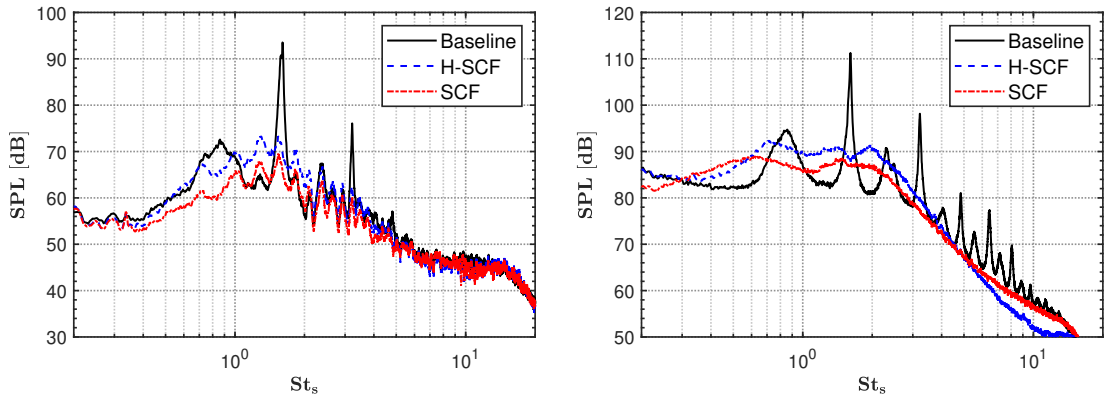


(a) Far-field, FF1

(b) Near-field, FG1

**FIG. 5:** Sound pressure level for all the tested configuration (a) far-field measurements FF1 at a distance 1 m away from the slat trailing edge and (b) near-field measurement FG1 on the main-element.

The tonal characteristics of the wall pressure spectra with multiple distinct narrowband peaks indicate the presence of cavity oscillations for the Baseline configuration, see Fig. 5. Additionally, these strong tonal peaks are also seen in the far-field noise measurements. The observed tonal peaks

are due to the flow-acoustic coupling between the slat cusp shear layer and its impingement on the slat trailing edge, leading to distinct tonal peaks. These tones can be accurately predicted using a simplified Rossiter mode equation (Eq. 15), as previously proven by Terracol *et al.* and other studies[20,24,54]. In line with Terracol's investigation[24], the discrete tonal frequencies from the flow interaction with the slat were predicted using,

$$f_n = n\frac{U_\infty}{L_a}\left(\frac{1}{M+\eta_l/\kappa_v}\right). \tag{15}$$

A simplified schematic and the parameters used in Eq. 15 by Terracol *et al.*[24] are shown and listed in Table III along with the parameters used in the current study. The local mean flow velocity data required for this prediction model were acquired from the PIV measurements by Kamliya *et al.* in previous studies[3,5,8,49]. It should be noted that according to Terracol *et al.*[24], the vortices originating from the slat cusp are convected along the main shear layer surrounding the main vortex core inside the slat cove, at a mean convection velocity ($U_v$). Although the flow is highly unsteady in the slat shear layer, following Terracol *et al.*[24], in the present study, the convecting velocity of the vortices in the slat shear layer was assumed to be constant and the average velocity was used in the Rossiter formula.

**TABLE III:** Simplified schematic of the tonal frequency prediction model by Terracol *et al.*[24], and the parameters used for the tonal peak frequency prediction in the present study for angle of attack $\alpha = 18°$.

| Schematic | Variables | Parameters | Values | Units |
|---|---|---|---|---|
| 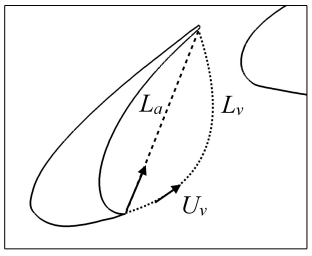 | $L_v$ | shear layer path length | 0.037 | m |
| | $L_a$ | acoustic path length | 0.035 | m |
| | $U_v$ | mean convection velocity | 18 | m/s |
| | $U_\infty$ | free-stream velocity | 30 | m/s |
| | $M$ | free-stream Mach number | 0.09 | - |
| | $\kappa_v$ | $= U_v/U_\infty$ | 0.60 | - |
| | $\eta_l$ | $= L_v/L_a$ | 1.06 | - |



The analytical prediction for the Baseline configuration at angle of attack $\alpha = 18°$ are presented in Table IV using Eq. 15 by Terracol *et al.*[24]. It was observed that Eq. 15 can predict the modes

**TABLE IV:** The tonal peaks observed for the Baseline case in the near-field and far-field measurements at angles of attack 18°.

| No. | $St_n$ | $St_s$ | Description | Experiment $f$ (Hz) | Analytical $f$ (Hz) |
|---|---|---|---|---|---|
| 1 | $St_1$ | 0.857 | mode 1 | 489.7 | 461.7 |
| 2 | $St_2$ | 1.611 | mode 2 | 920.6 | 923.3 |
| 3 | $St_3$ | 2.303 | mode 3 | 1316 | 1385 |
| 4 | $St_4$ | 3.212 | $= 2St_2$ | 1835.4 | 1846.6 |
| 5 | $St_5$ | 4.056 | $= St_3 + St_2$ | 2317.7 | 2308.3 |
| 6 | $St_6$ | 4.841 | $= 3St_2$ | 2766.2 | 2769.9 |

accurately, thereby, confirming that the modes are generated from the acoustic feedback mechanism. In Fig. 5 and Table IV, the narrowband peaks from $St_2$ to $St_6$ are distinct with high energy. Whereas, the $St_1$ peak observed in the results is more of a broadband hump that is well distributed between $St_s = 0.5 - 1$. This combined nature of the $St_1$ peak was identified and documented by Kamliya *et al.*[4]. However, the nature and source of this broadband hump were not identified. In the following sections, the nature and source of this broadband hump will be further analyzed and its difference from the Rossiter mode will be documented.

## B. Wall pressure single-point statistics

### *1. Power spectral density*

As a part of this experimental campaign to isolate the broadband hump at $St_1$, several remote sensors (M1-M4 and S1) were connected to the surface pressure ports on the main-element and slat in the slat cove region. The locations of these remote sensors are detailed in Fig. 4 and Table II. The SPL spectra for the remote sensors on the main-element M1-M4 and on the slat S1 for the tested Baseline, H-SCF, and SCF configurations are presented in Fig. 6. At first glance, the Baseline configuration clearly shows several tonal peaks related to the Rossiter modes arising from the feedback between the slat cusp and slat trailing edge. The sound pressure level increases from remote sensor location M1 to M3 and decreases past the slat gap at M4. Overall, the highest sound pressure levels were observed at M3. At location S1 on the pressure side of the slat, lower sound

pressure levels were observed compared to the other remote sensor locations. When considering the broadband hump between $St_s = 0.5 - 1$, the highest sound pressure levels were observed at both the M2 and M3 locations with similar magnitude, and the lowest sound pressure levels at the slat sensor location S1.

The use of slat cove fillers eliminated the tonal peaks observed in the Baseline configuration. Overall, the remote sensors M1 and M4 have similar spectral levels at $St_s < 1.5$ with M4 having higher spectral levels at $St_s > 1.5$ for both the presented slat cove filler configurations. The remote sensors M2 and M3 show similar levels at $St_s < 1$ but at $St_s > 1$, M3 shows higher spectral levels for both the cove filler configurations. Ultimately, the unsteady surface pressure results have shown high levels of energy at M3 compared to the other measurement locations for all the presented configurations. The higher energy levels observed at M3 cannot confirm the location at which the broadband hump is being generated within the slat cove region, therefore, further analysis is required to isolate the source of the broadband hump ($St_1$).

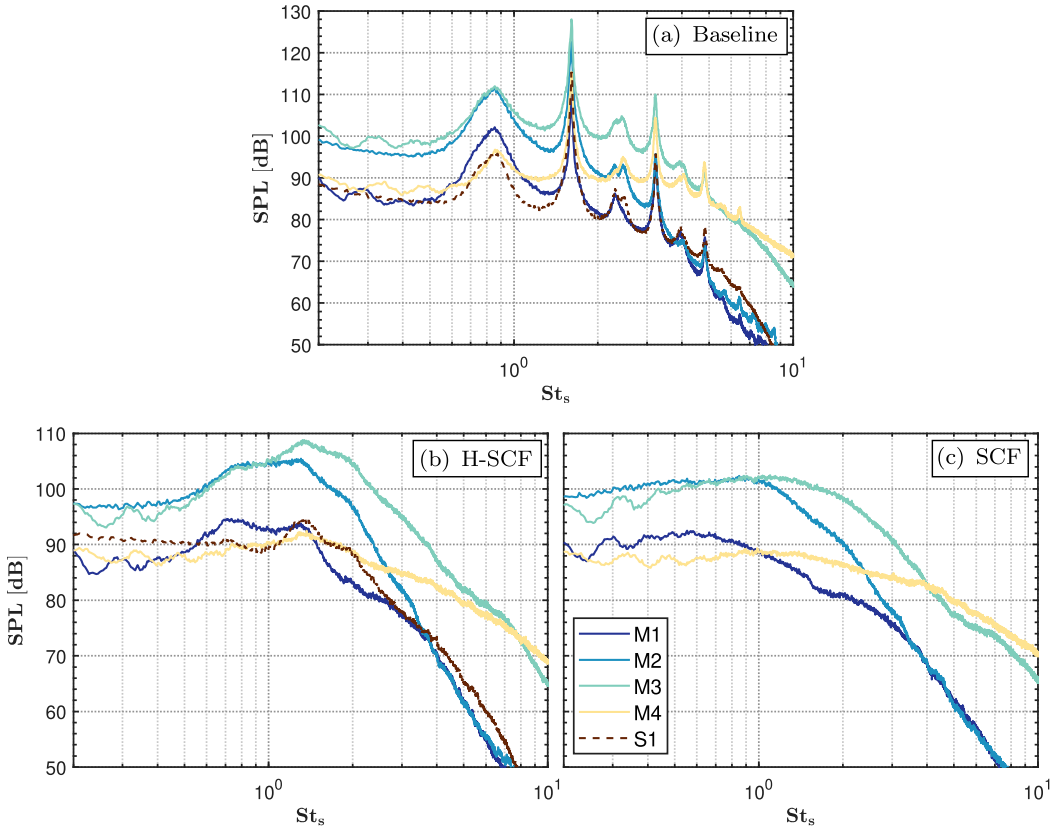


**FIG. 6:** Near field energy spectra for the surface pressure transducers shown in Fig. 4: (a) Baseline, (b) Half slat cove filler (H-SCF), and (c) Slat cove filler (SCF).

### C. Wall pressure two-point statistics

#### 1. *Cross-correlation analysis*

Two-point statistics of the pressure signals were computed using the auto and cross-correlation between two remote sensors. The auto- and cross-correlations were computed using,

$$R_{p_i p_j}(\tau) = \frac{\overline{p_i(t+\tau)p_j(t)}}{p_{i_{rms}} p_{j_{rms}}}, \quad \text{for } p_i = \text{ M1 and } p_j = \text{ M1, M2, M3, M4,} \tag{16}$$

where $p_i$ and $p_{i_{rms}}$ are the surface pressure and surface pressure root-mean-square of the reference remote sensor signals (M1), $p_j$ and $p_{j_{rms}}$ are the surface pressure and surface pressure root-mean-square of the downstream remote sensor signals at various locations along the chord, $\tau$ is the time-delay and the time average is represented by the overbar.

The auto-correlation results ($R_{p_i p_j}(\tau)$) as a function of the normalized time-delay $\tau^* = \tau U_\infty / c_s$ for the three tested configurations at various remote sensor locations on the main-element are presented in Fig. 7. At first glance, it is evident that the flow exhibits different characteristics at different remote sensor locations for the three presented configurations. For the Baseline, M1 and M4 exhibit a fast decaying periodic behavior, whereas M2 and M3 exhibit a slow decaying periodic behavior with a Gaussian shape having a low decay rate. Therefore, this behavior is suggestive of a strong vortex shedding. Furthermore, this can be confirmed by calculating the frequency ($\tau^*_{vs}$) from the two peaks of the $R_{p_i p_j}(\tau)$ as demonstrated by Kamliya *et al.*[4]. The calculated time-delay $\tau^*_{vs} = 0.6626$ corresponds to $St_{vs} = 1.51 \approx St_2$, which is the vortex shedding frequency. This frequency further corresponds to the tone seen in the SPL plots in Figs. 5 and 6. In the case of the H-SCF configuration, at M2 and M3, the periodic behavior decays rapidly, indicating very low energy of the vortex shedding. Moreover, the periodic behavior is completely absent at all the remote sensor locations, suggesting the absence of a vortex shedding for the SCF configuration.

The results of the cross-correlation of the surface pressure fluctuations with reference to the microphone on the main-element, M1 are presented in Fig. 8. As expected, the streamwise cross-correlation results for the remote sensors on the main-element (M1-M4) confirm the difference in the time-lag between the various remote sensors. For the Baseline configuration, the time-lag increases with the distance between the remote sensors. The H-SCF configuration shows a considerable increase in the time-lag between the remote sensors on the main-element and also has

increased the time-lag than that of the Baseline. In the case of SCF configuration, the time-lag further increases compared to both the Baseline and H-SCF configurations. Additionally, the cross-correlation magnitude between the M1 and M4 is reduced substantially for the H-SCF configuration and is completely absent for the SCF configuration. This is likely due to the interference of the cove fillers on the coherent structures passing between M1 and M4. The use of cove filler appears to interfere with the turbulent structures making the cross-correlation shape larger ($\tau^* = \tau U_\infty / c_s$) seemingly due to the breaking of coherent structures.

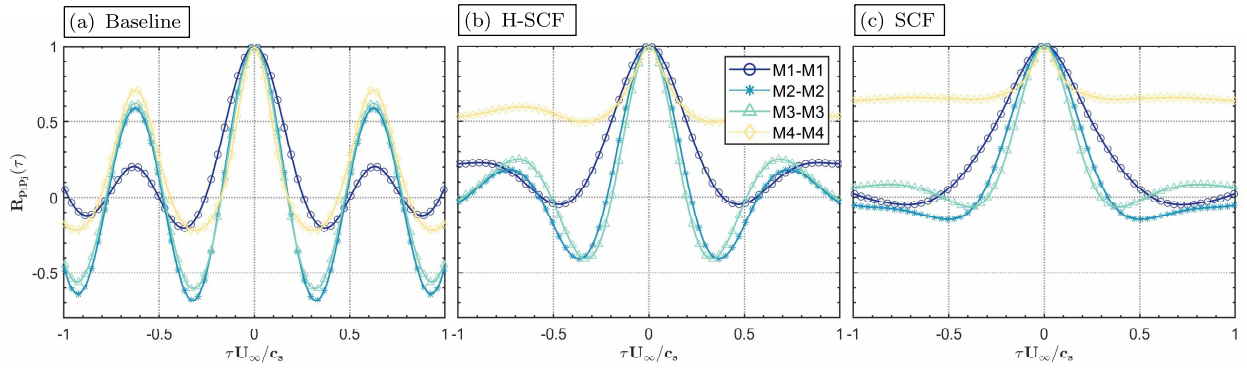


**FIG. 7:** Auto-correlation of the surface pressure fluctuations for the remote sensors on the main-element: (a) Baseline, (b) H-SCF, and (c) SCF.

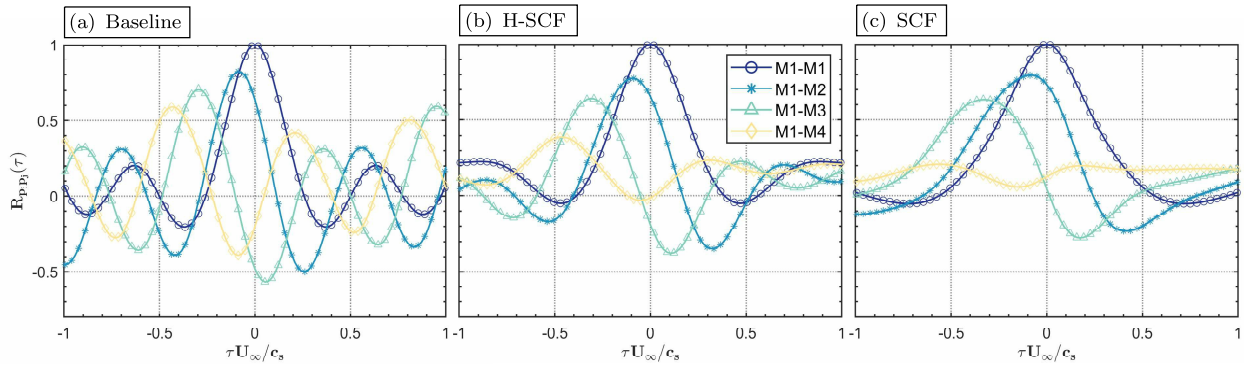


**FIG. 8:** Cross-correlation of the surface pressure fluctuations for the remote sensor with M1 as reference: (a) Baseline, (b) H-SCF, and (c) SCF.

The coherence function calculates the phase correlation between two different remote sensors averaged over time. The coherence between the surface remote sensors can be obtained using the

following equation,

$$\gamma^2_{p_i p_j}(f) = \frac{|\ \Phi_{p_i p_j}(f)\ |^2}{\Phi_{p_i p_i}(f)\Phi_{p_j p_j}(f)} \quad \text{for } p_i = \text{ M1 and } p_j = \text{ M1, M2, M3, M4,} \tag{17}$$

where the symbol $|\square|$ denotes the absolute value, $p_i$ is the reference remote sensor signal (M1), $p_j$ is the remote sensor signal at various locations within the slat cove region and $\Phi_{p_i p_j}$ is the cross-spectral density between two pressure signals, $p_i$ and $p_j$. The results for the near-field coherence of the pressure signals collected within the slat cavity region with M1 as the reference transducer, are presented in Fig. 9.

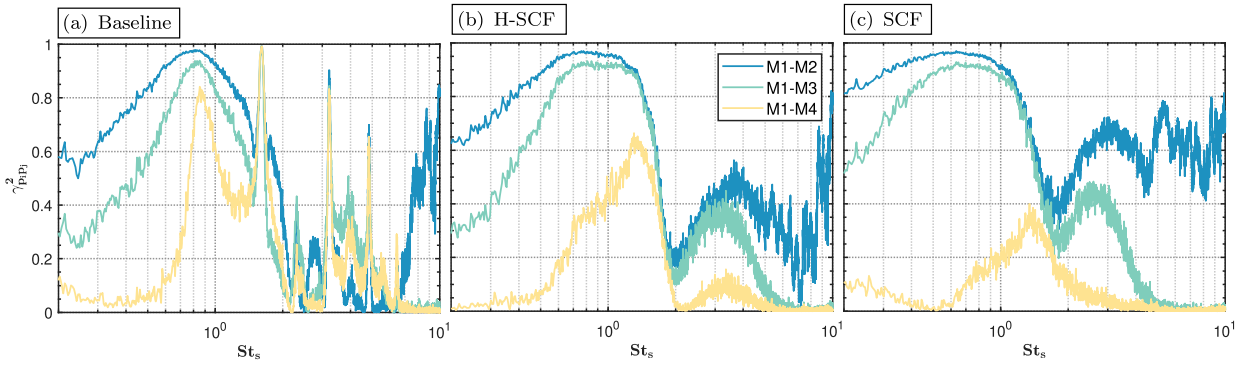


**FIG. 9:** Coherence of the surface pressure fluctuations between the remote sensor M1 and the following remote sensors on the main-element: (a) Baseline, (b) H-SCF, and (c) SCF.

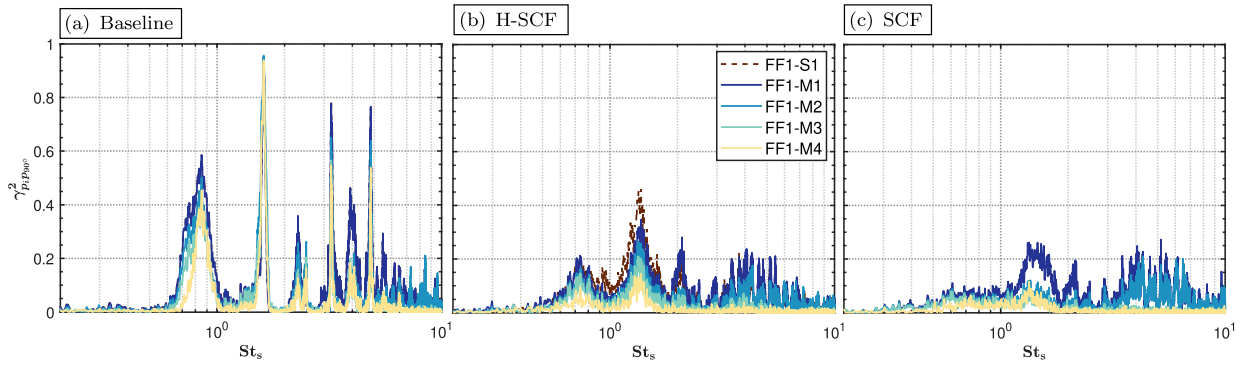


**FIG. 10:** Coherence of the surface pressure fluctuations between the far-field microphone FF1 located at 1 m away from the slat trailing edge and the various remote sensors on the high-lift airfoil: (a) Baseline, (b) H-SCF, and (c) SCF.

The results of the streamwise coherence of the remote sensors present a high level of coherence for the even narrowband peaks ($St_{2,4,6}$) and low coherence for the odd narrowband peaks ($St_{3,5}$)

between the main-element remote sensors (M1-M4). In line with the discussion from the previous sections, from the following results in Fig. 9, it was observed that the broadband hump was clearly of a different nature. Accordingly, the coherence results in the case of M1-M2/M3, the results exhibit a high coherence level between $St_s = 0.6 - 1$, whereas in the case of M1-M4, a narrower peak with high levels of coherence is observed exclusively between $St_s = 0.8 - 1$. This shows that even though the peak $St_1$ might be influenced by the Rossiter modes, the broadband hump is not generated by them and is further confirmed by the cove filler coherence results. For the H-SCF and SCF configurations, high coherence at $St_s < 1$ for M1-M2 and M1-M3 are observed. Interestingly, in the case of M1-M4, the narrow peak observed for the Baseline configuration is absent for both the cove filler configurations with the SCF configuration having very low coherence. However, for both the H-SCF and SCF configurations a peak in the coherence level can be found at $St_s = 1.6$.

In order to understand the far-field propagation effects of the identified wall pressure signatures, the magnitude-square coherence between the wall pressure and far-field signals were calculated and presented in Fig. 10. The results of the near- to far-field coherence presented in Fig. 10 show a very high level of coherence for a series of narrowband peaks for the Baseline configuration. Furthermore, high coherence levels were observed for the even narrowband peaks ($St_{2,4,6}$) relative to the odd narrowband peaks ($St_{1,3,5}$) at all the remote sensor locations. Additionally, high levels of coherence of up to 0.6 were observed for $St_s = 0.7 - 0.9$, thus clarifying the presence of Rossiter mode at $St_1$. Moreover, this gives an insight into the broadband hump as the far-field coherence is narrower when compared to the streamwise coherence results seen earlier in Fig. 9. In the case of the slat cove filler configurations, low coherence levels are detected for the entire bandwidth with values less than 0.2. For the H-SCF configuration, marginally increased coherence levels with values of up to 0.4 are found at about $St_s = 1.6$. The SCF configuration has the lowest coherence levels compared to all the configurations except for a small broadband hump at about $St_s = 1.6$. It is noteworthy that for the SCF configuration, the broadband hump at $St_1$ has no coherence with the far-field noise, which suggests that the broadband hump is due to the non-propagating hydrodynamic energy field within the slat cove region.

### 2. *Wavelet analysis*

In the present study, the continuous wavelet transform ($CWT$) is employed to capture the local oscillating features of the remote sensor signals in the time-frequency plane, thereby enabling us to observe the temporal characteristics of the pressure fluctuations along with its associated frequency. The $CWT$ consists of a signal projection over a basis of support functions provided by the translation and dilatation of a mother wavelet function and it is defined[55,56] as,

$$W(s,t) = C_{\psi}^{\frac{-1}{2}} \int_{-\infty}^{\infty} p(\tau)\psi^*\left(\frac{t-\tau}{s}\right), \tag{18}$$

where $s$ is the scale dilatation parameter corresponding to the width of the wavelet, $\tau$ is the translation parameter corresponding to the position of the wavelet, $C_{\psi}^{\frac{-1}{2}}$ is a constant that takes the mean value of $\psi(t)$ into account and $\psi^*\left(\frac{t-\tau}{s}\right)$ is the complex conjugate of the dilated and translated mother wavelet $\psi(t)$. The Morlet kernel was chosen as the mother wavelet, as reported analytically in previous studies[4,55].

The contours of the wavelet coefficient moduli for the near-field remote sensor on the main-element (M3) are presented in Fig. 12 for all the tested configurations. Although the analysis was carried out for all the remote sensors, the results are presented only for M3 due to increased fluctuations at this location as will be shown later. In principle, the wavelet coefficients remain small if the fluctuations at a given time are smooth, and their value increases locally for large fluctuations, i.e., irregular structures. As a consequence, wavelet coefficients do not correspond to the entire signal's strength but to the fluctuations at a given scale and a given point. Following that, the Baseline configuration shows a high wavelet coefficient at the vortex shedding frequency of $St_s = 1.61$ for all the remote sensor locations. For the frequencies of interest, $St_1$ and $St_2$, the highest wavelet coefficient was found at the location M3 amongst all the other remote sensor locations. For the H-SCF and SCF configurations, it is observed that the peak with increased fluctuations at $St_2$ is absent. Overall, the results show high wavelet coefficient levels at M3 compared to all the other remote sensor locations for all the tested configurations.

The importance of phase-space characteristics to analyze turbulence is well demonstrated by Farge[56]. Accordingly, the phase-space characteristics of the pressure fluctuations along with the real part of the wavelet coefficients for the remote sensor M3 on the main-element are presented in Fig. 13. Throughout the discussion, it is preferred for the readers to refer to the real part of

the wavelet coefficients (see Figs. 13a, 13b and 13c) along with the phase-space characteristics (see Figs. 13d, 13e and 13f) for better interpretation of the results. To better visualize the phase-space characteristics, the results are presented for a relatively short time period of 0.33 seconds. At first glance, all three configurations evidently show a different phase-space characteristic pattern with a lack of background noise. These patterns can further be separated into characteristic classes (repetitive and cone-like patterns) and can then be analyzed by class. The Baseline configuration at $St_2$ shows multiple repetitive patches in both the real part of the wavelet coefficients and the phase-space. This phase-space behavior is expected of a turbulent field with a superposition of wave-packets, such as eddies[56]. As defined by Farge[56], the horizontal length of these patches corresponds to the spatial support of the eddies and the vertical length to the frequencies characterizing each excited wave-packet. The phase-space behavior at $St_2$ with repetitive patches also corresponds to the vortex shedding frequency. The phase-space behavior at the broadband hump $St_s = 0.5 - 1$ displays energy density distributed among cone-like patterns, suggestive of the presence of coherent structures with each cone pointing to an excited structure[56]. The spatial support (width) of these cones at the broadband hump $St_s = 0.5 - 1$ is significantly larger than the repetitive patches seen at $St_2$, yet again clarifying the different nature of the broadband hump at $St_s = 0.5 - 1$. In the case of the H-SCF and SCF configurations, the energy density is distributed in cone-like patterns of different sizes at varying bandwidths that points to the presence of various coherent structures. The amplitude of the real part of the wavelet coefficients show that these coherent structures possess lower energy for the slat cove filler configurations compared to the Baseline configuration.

Power spectral density of the wavelet coefficient moduli ($|W_{St}|$) at frequencies of interest would further aid in the understanding of the tone generation mechanism. The results of the amplitude of the wavelet coefficient moduli ($E(|W_{St}|)$) are presented in terms of the slat chord-based Strouhal number ($St_s$) in Fig. 14 at frequencies listed in Table. IV. For the Baseline configuration, the results show that the modes $St_3, 4, 5$ and 6 are modulated by $\Delta St_s = 1.61$. A broadband hump with a peak at $St_s = 0.7$ is observed for the mode $St_3$ at the remote sensor location M3. Overall, these results identify the Rossiter mode concealed within the broadband hump. On the contrary, the H-SCF and SCF configurations do not show any amplitude modulation at any of the remote sensor locations for all the frequencies considered here.

To better understand the fluctuating characteristics of the surface pressure at various remote sensors, the statistical distribution of the fluctuating properties using the wavelet coefficient moduli

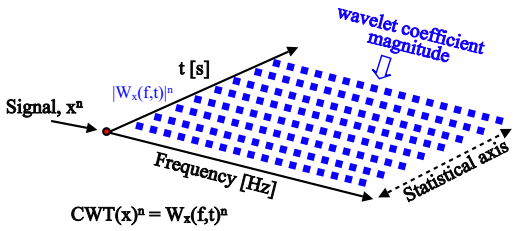


**FIG. 11:** Schematic of the statistical analysis of the wavelet coefficient moduli.

($|W_x|$) at every frequency is presented[17,57]. A simple schematic of the statistical analysis employed in this study is shown in Fig. 11. It is well known that the Fourier spectra of a given signal can be recovered by integrating the wavelet coefficient moduli in time, providing spectra less affected by statistical uncertainties[56]. Following a similar strategy, in the present study, a detailed statistical analysis of the wavelet coefficient moduli was carried out over a time period of 120 seconds. The statistical representation of the wavelet coefficient moduli is presented in terms of the arithmetic mean ($\mu(|W_x|)$), standard deviation ($\sigma(|W_x|)$) and coefficient of variation ($CV(|W_x|)$), to characterize the fluctuations in the flow. They are employed in the current study, with $N$ as the total number of time steps,

$$\mu(|W_x|) = \frac{\Sigma_{i=1}^{N}|W_x|}{N}, \tag{19}$$

$$\sigma(|W_x|) = \sqrt{\frac{\Sigma_{i=1}^{N}(|W_x|_i - \mu(|W_x|))^2}{N}}, \tag{20}$$

$$CV(|W_x|) = \frac{\sigma(|W_x|)}{\mu(|W_x|)} \times 100. \tag{21}$$

The statistical representation of the fluctuating properties calculated from the continuous wavelet analysis is presented in Fig. 15 in terms of frequency. The mean ($\mu(|W_x|)$) and standard deviation ($\sigma(|W_x|)$) of the wavelet coefficient moduli for various remote sensors are presented in the first and second row of Fig. 15, respectively. At first glance, the remote sensor M3 shows a substantial increase for $\mu(|W_x|)$ and $\sigma(|W_x|)$ compared to the other remote sensor locations. For the Baseline case, increased values of $\mu(|W_x|)$ at M3 are observed with a peak at $St_2$. Although all the remote sensors record this primary peak, M3 possesses the highest fluctuation compared to the other locations. In addition to this, the broadband hump at $St_s = 0.5 - 1$ also shows increased $\mu(|W_x|)$

levels at M3 compared to the readings at other locations. The results for the H-SCF configuration (Fig. 15b) shows reduced fluctuations compared to the Baseline, whereas the SCF configuration shows further reductions compared to the H-SCF configuration. The $\sigma(|W_x|)$ for the Baseline case displays two peaks at $St_1$ and $St_2$ for the M2 and M3 remote sensor locations. Interestingly, this double peak (Fig. 15d) is not observed at any other remote sensor location, indicating that the pressure fluctuations for the broadband hump ($\approx St_1$) are spread far from the mean distribution at M2 and M3 with relatively higher values at M3. The $\sigma(|W_x|)$ for M3 at $St_1$ shows marginally larger values than at $St_2$. Ultimately, the $\sigma(|W_x|)$ results show that the generation of the broadband hump is at the proximity of M3 adjacent to the slat gap. Conversely, these two peaks at $St_1$ and $St_2$ in $\sigma(|W_x|)$ are not detected at M4. Contrary to the Baseline configuration, the $\sigma(|W_x|)$ for the H-SCF and SCF configurations do not show any characteristic behavior, instead follow the trends similar to that of the $\mu(|W_x|)$.

The coefficient of variation $CV(|W_x|)$ is the ratio of the standard deviation to the mean, which essentially shows the fluctuation intensity of the pressure signals at a given frequency in terms of percentage[17,58]. The higher the $CV(|W_x|)$, the greater the level of dispersion around the mean. The $CV(|W_x|)$ is presented to compare the pressure fluctuations at various pressure transducers on the same relative scale (ratio). The $CV(|W_x|)$ in Fig. 15 is presented in terms of percentage and shows the relative dispersion of the pressure fluctuations. The frequencies with smaller $CV(|W_x|)$ are less dispersed compared to the frequencies with a larger $CV(|W_x|)$. For the Baseline, it is evident from the $CV(|W_x|)$ that $St_1$ with larger values (up to 65%) is of a different nature compared to the $St_2$ with lower values (up to 20%) for all the locations on the slat and main-element. Interestingly, at M4 the $CV(|W_x|)$ is low at $St_1$ compared to all the sensors. In the case of the H-SCF configuration, the changes in $CV(|W_x|)$ remain low for all the frequencies and remote sensor locations except for S1 at frequencies $St_s > 5$. Finally, for the SCF configuration, the changes in $CV(|W_x|)$ remain relatively low for the entire bandwidth at all the locations compared to Baseline and H-SCF configurations. These observations reaffirm that the application of the slat cove filler changes the flow structure within the slat region entirely and more importantly the $St_1$ and $St_2$ are of a different nature.

The phase-space analysis (see Fig. 13) and stochastic analysis (see Fig. 15) of the wavelet coefficient moduli evidently shows that the $St_1$ and $St_2$ are of a different nature. Furthermore, from $\sigma(|W_x|)$ it is clear that the broadband hump ($St_s = 0.5 - 1$) is generated at the vicinity of the slat gap (see Fig. 4 and Fig. 15d), it should also be noted that M3 showed the highest energy in Sec.

IV B 1 (see Fig. 6) and also in the continuous wavelet transform scalogram (see Fig. 12).

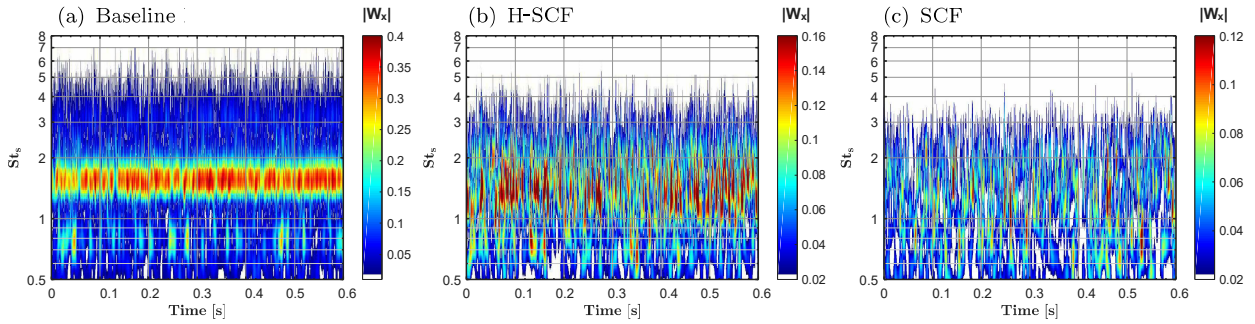


**FIG. 12:** Wavelet scalogram of a segment of a pressure signal obtained at remote sensor location M3: (a) Baseline, (b) H-SCF, and (c) SCF.

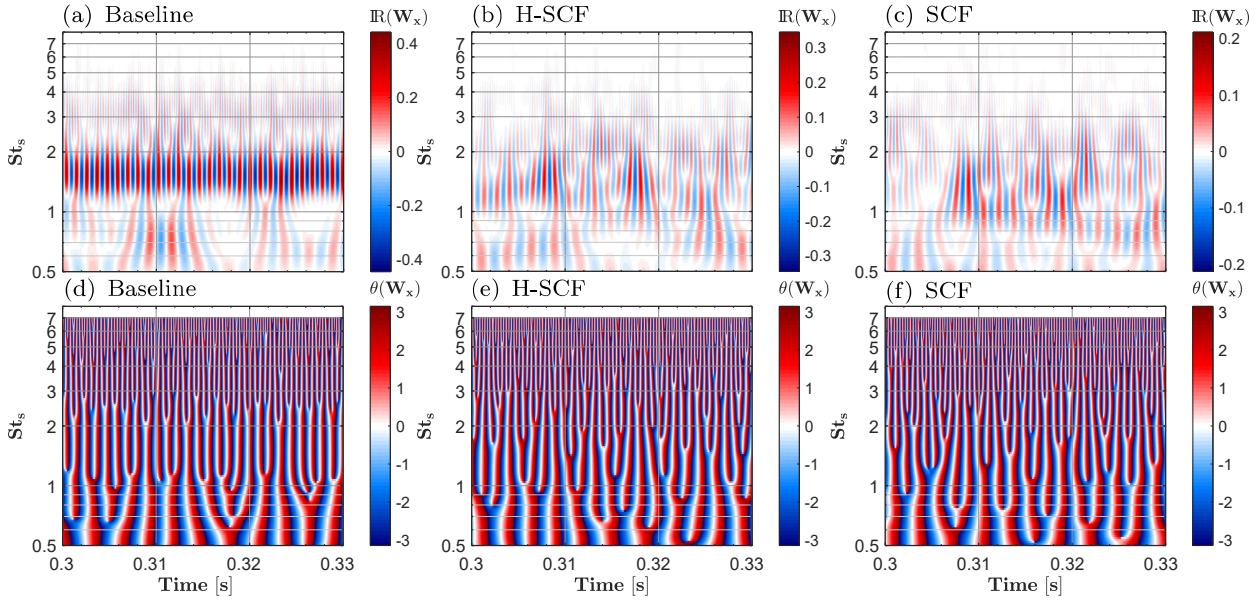


**FIG. 13:** The real part of the wavelet coefficient ((a) Baseline, (b) H-SCF, and (c) SCF) and the phase-space characteristics ((d) Baseline, (e) H-SCF, and (f) SCF) of the surface pressure fluctuations at M3 from the continuous wavelet transform.

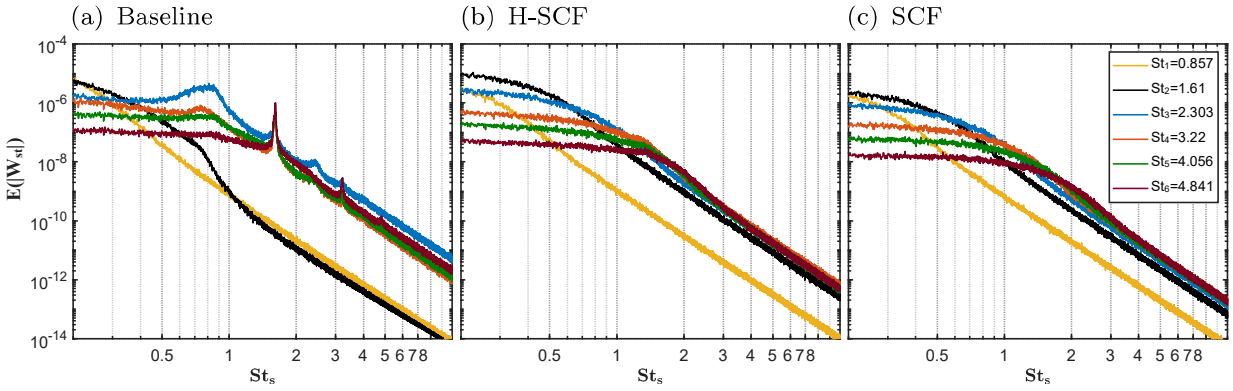


**FIG. 14:** Power spectral density of time signal and wavelet coefficient at selected resonance frequencies at location M3: (a) Baseline, (b) H-SCF, and (c) SCF.

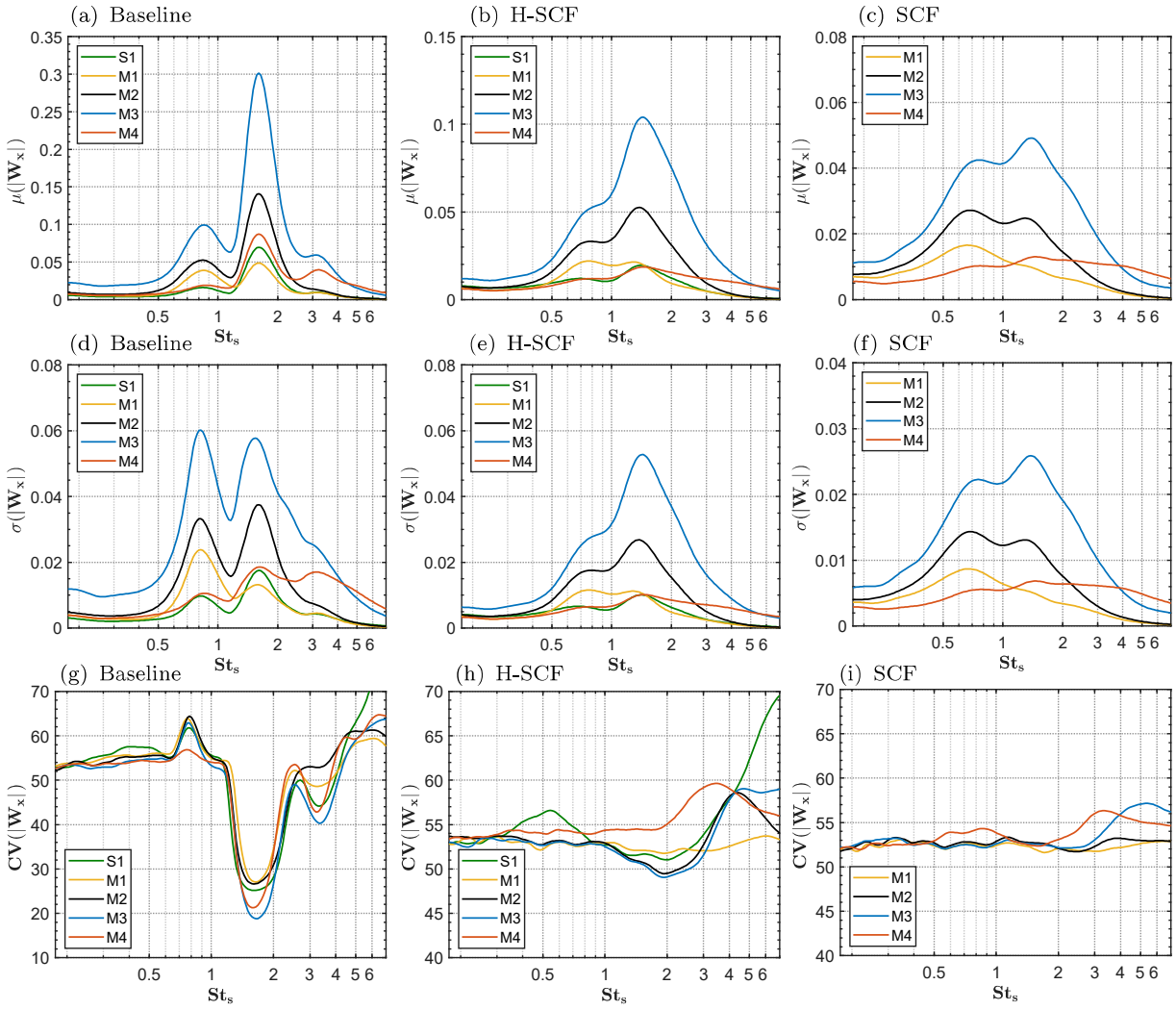


**FIG. 15:** Stochastic analysis for the various frequencies of interest at various remote sensor locations: (a) $\mu(|W_x|)$, Baseline, (b) $\mu(|W_x|)$, H-SCF, (c) $\mu(|W_x|)$, SCF, (d) $\sigma(|W_x|)$, Baseline, (e) $\sigma(|W_x|)$, H-SCF, (f) $\sigma(|W_x|)$, SCF, (g) $CV(|W_x|)$, Baseline, (h) $CV(|W_x|)$, H-SCF, and (i) $CV(|W_x|)$, SCF.

## V. MODE DYNAMICS

Although the underlying physics of the slat tones and the broadband hump generation observed for the Baseline configuration appear to be complex, it can be better identified by using lower-order models governed by a few modes to capture the dominant behavior of the system. These modes are commonly referred to as coherent spatio-temporal structures[59]. In order to extract the most dominant characteristics of the system, to find the underlying patterns, and to predict the system dynamics, the data-driven technique Dynamic Mode Decomposition (DMD) was employed. It should be emphasized that in the present study the DMD technique is not used in the conventional way commonly used in fluid mechanics but it is used as a data-driven analysis tool to capture time dependence of a point in geometrical space, as demonstrated by Kutz *et al.*[50,51]. The DMD technique is applied on large time evolution data sets of the wavelet coefficient moduli ($|W_x|$) calculated from different remote sensors within the slat cove region where the slat Strouhal number ($St_s$) and sensor locations are treated as spatial measurements. The DMD analysis aids us to better interpret the $St_s$ evolution in time as the derived modes of the $St_s$ would be associated with their damped (or driven) sinusoidal behavior in time and geometrical space. It is well known that the standard DMD algorithm is sensitive to its eigenvalue spectrum to noisy data[50,51]. Therefore, the method of averaging the forward and backward DMD introduced by Dawson *et al.*[60] to remove the systematic bias in the DMD eigenvalues caused by the measurement noise was also considered. However, the characteristics of the modes of interest showed negligible difference compared to the standard DMD procedure as a result of the intensity of the dominant characteristics being higher than the signal noise levels. Ultimately, the standard DMD algorithm was applied to $8.19 \times 10^5$ snapshots of the wavelet coefficient moduli from various normalized remote sensor signals of the Baseline configuration. For the sake of brevity, the results are presented only for Baseline configuration since the slat cove filler configurations lacked dominant dynamic behavior that the DMD procedure could capture.

The magnitude of the Ritz value ($\lambda_r$ and $\lambda_i$) for the first 30 modes relative to the unit circle are presented in Fig. 16. The discrete-time eigenvalues typically lie on the unit circle indicating the neutral stability of the corresponding DMD spatial mode $\Phi$, as seen in the continuous-time plot. The color of the markers indicates the amplitude of the eigenvalue in the sequential data where darker colors indicate higher amplitude. Furthermore, the oscillatory frequency of the modes could

be found using the phase of the $\lambda_i$. The eigenvalues $\lambda$ are mapped logarithmically and normalized by $\Delta t$ to get $\omega = log(\lambda)/(2\pi\Delta t)$ resulting with the imaginary component of $\omega_i$ as the frequency of oscillation in units of cycles per second. Although the dynamics of transients are captured quite well, the eigenvalues with small real parts decay quickly, which is in line with previous studies[61].

The result of the first six DMD modes of the $St_s$ evolution over time at various remote sensor locations for the Baseline configuration is presented in Fig. 17. Since the $St_s$ evolution over time has complex translation dynamics, it would require several modes to get the precise dynamics with all the embedded low-rank modes. Nevertheless, only the first few modes are presented here to represent the most important dynamic characteristics of the $St_s$. The results of mode-1 show the sinusoidal behavior of the $St_2 = 1.6$ at location M2 oscillating between $St_s \approx 1.1$ and 2.1, which is due to the vortex shedding phenomenon. At mode-2, phase oscillations corresponding to the vortex shedding were observed at location M1. As expected, none of the vortex shedding associated phase oscillation could be observed at locations M3 and M4 for any of the presented modes as the shear layer encompassing the vortex shedding impinges on the slat trailing edge and does not pass through the slat gap. The results of the remaining modes show that $St_1$ ($St_s = 0.5 - 1$) moves periodically with a fixed phase relation between M2 and M3. This yet again supports the hypothesis that the $St_1$ is different to $St_2$ and that the broadband hump ($St_1$) translates in geometrical space through the slat gap past location M3, whereas the dominance of $St_2$ is not seen past M2 in the first few modes.

It is well established that the standard DMD method is incapable of capturing transient phenomena such as the on-off nature of the modes[50,51], as seen from the DMD results presented above. The multi-resolution DMD (mrDMD)[50] has been shown to effectively decompose the dynamics into different timescales, isolating the transient and intermittent patterns. Additionally, it has also been proven to be very successful in separating slow and fast modes even with the presence of background noise. Therefore, the mrDMD, capable of separating the multi-scale spatio-temporal features to uncover multi-scale structures, were applied to the judiciously truncated data set consisting of wavelet coefficient moduli of the various remote sensors. The mrDMD was first applied to the data set truncated between $St_s = 0.5 - 1$ (window 1), which encompasses the first slat mode of interest $St_1 = 0.857$. In a similar fashion, the mrDMD was then applied to the data truncated between $St_s = 1 - 2$ (window 2), which encompasses the slat second mode $St_2 = 1.6$ for a time period of 3 s. Finally, the mrDMD results of both the judiciously truncated windows 1 and 2 for

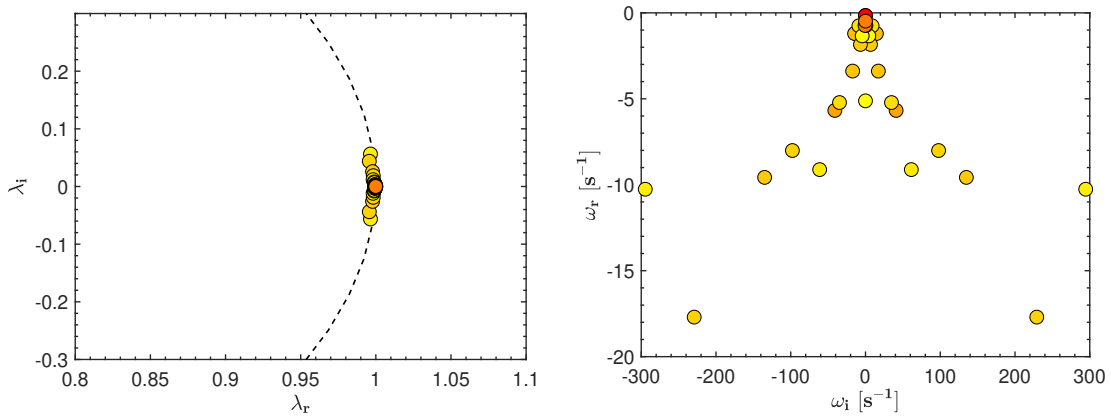


(a) Ritz value

(b) DMD spectrum

**FIG. 16:** DMD eigenvalues for the first 30 modes of the $St_s$ evolution shown in Figure 17. The discrete time eigenvalues $\lambda$ relative to the unit circle and the eigenvalues presented in continuous time as $\omega = log(\lambda)/(2\pi\Delta t)$ coloured by their amplitude: (a) Ritz value and (b) DMD spectrum.

the Baseline configuration at remote sensor location S1 are presented in Fig. 18 for a model number and decomposition level of 10 and 8, respectively ($\phi_{10}^{(8,j)}$). For window 1, the mrDMD results show that the $St_1$ has a strong pulsation with a frequency of 10 Hz to 21 Hz at two instances over a time period of three seconds. The $St_1$ also portrays a slightly faster pulsation with a frequency of 21 Hz to 41 Hz but with reduced modal intensity occurring in pairs at random instances over the evaluated time period. Subsequently, the mrDMD results for the window 2 ($St_2$) show high modal energy at the first level. This was expected as the tonal characteristics were present throughout the time signal. In some instances, a low-intensity pulsation of the $St_2$ occurs with a frequency of 42 Hz to 85 Hz. The mrDMD results have shown that there exists a strong pulsation of the broadband hump. Overall, the slat modes ($St_1$&$St_2$) possess distinct intermittent characteristics, which were identified by the mrDMD method.

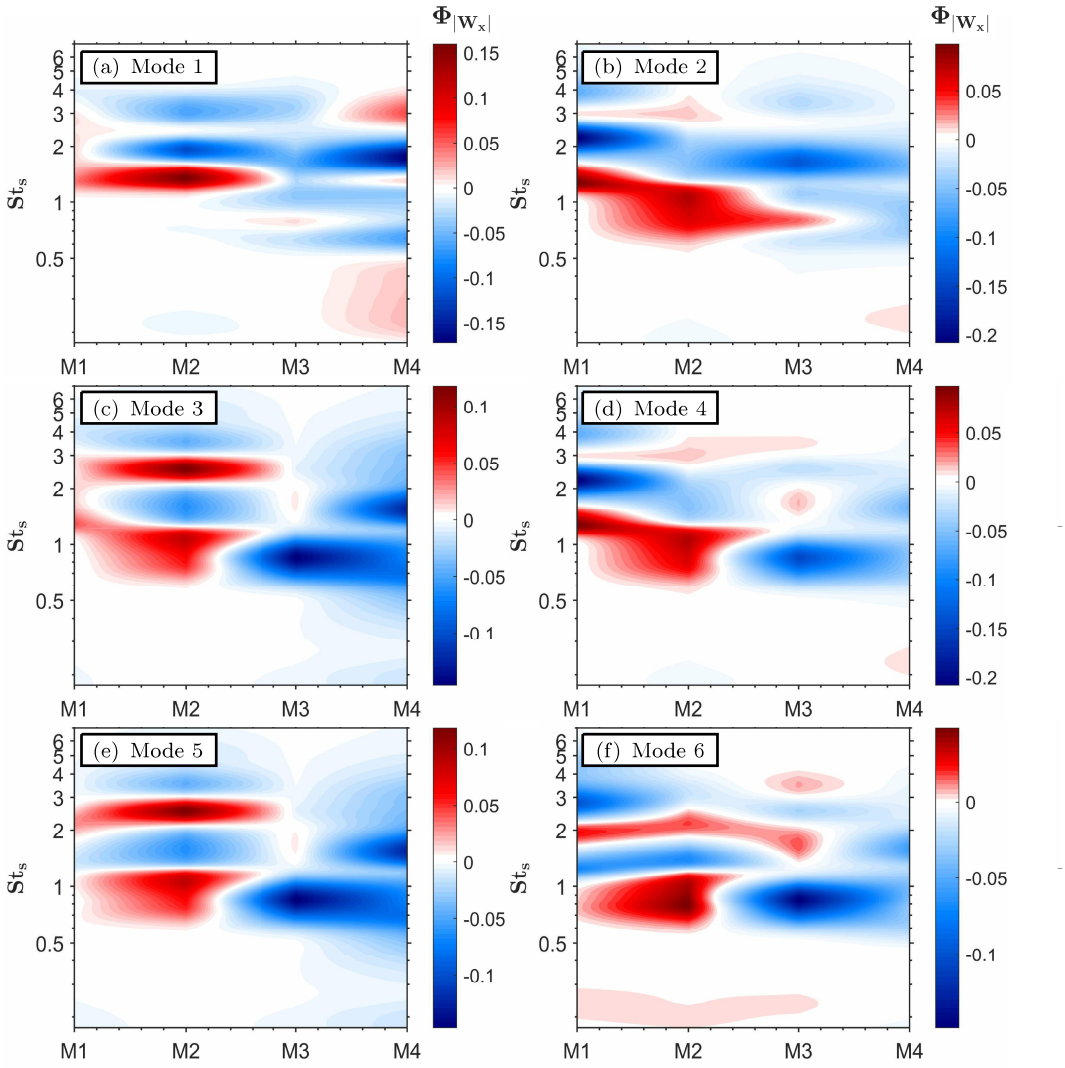


**FIG. 17:** The contours of the first six DMD modes of the $St_s$ evolution in time at various remote sensor locations for the Baseline configuration: (a) Mode-1, (b) Mode-2, (c) Mode-3, (d) Mode-4, (e) Mode-5 and (f) Mode-6.

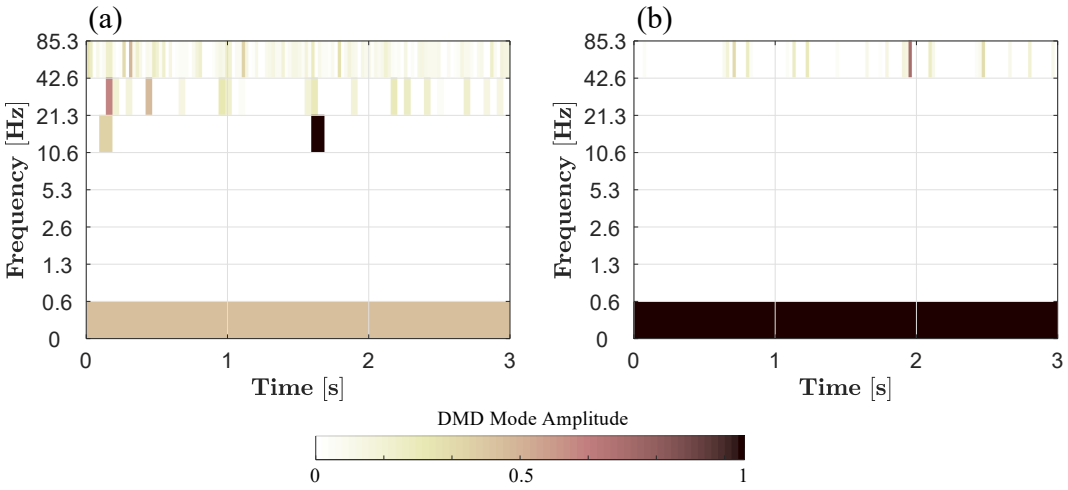


**FIG. 18:** The multi-resolution view of power of the recurring events at (a) window 1 ($St_s = 0.5 - 1$) and (b) window 2 ($St_s = 1 - 2$) as it varies in time and in frequency for the Baseline configuration at remote sensor location on the slat S1.

## VI. CONCLUSION

An experimental study with a 30P30N three-element high-lift airfoil fitted with two different types of slat cove fillers was carried out in the aeroacoustic facility at the University of Bristol. Unsteady surface pressure measurements within the slat cove were carried out using several remote sensors. The results are presented for all the tested configurations at the angle of attack $\alpha = 18°$ for a free-stream velocity of $U_\infty = 30$ m/s, corresponding to a chord-based Reynolds number of $Re_c = 7 \times 10^5$. As expected, the slat cove filler configurations show reduced noise levels in both the near- and far-field measurements at low-frequency and elimination of the characteristic tonal noise generated by the slat. The near-field spectra confirmed that the tones were indeed a result of cavity resonance and Rossiter modes. Intermittent events induced by the resonant mechanism between the slat and its trailing edge demonstrated a substantial difference for all the configurations with notable behavior close to the slat gap. The auto-correlation of the near-field surface pressure fluctuations for both the slat cove filler configurations indicated suppression of the strong vortex shedding. Furthermore, in the slat cove region, the streamwise correlation between the remote sensors pointed out possible interference of the slat cove fillers with the turbulent structures making the cross-correlation shape larger probably due to the break-up of coherent structures. Interestingly, the streamwise coherence indicated that the broadband hump is different from that of the high-order Rossiter modes. The near- to far-field pressure coherence results exhibited high coherence for the narrowband peaks for the Baseline configuration, whereas for the slat cove filler configurations, an overall low coherence was observed. To identify the source of the broadband hump, wavelet analysis using continuous wavelet transform was carried out. The results from the wavelet analysis showed that high levels of wavelet coefficient moduli for the frequencies of interest ($St_s = 0.5 - 1$) were observed at the remote sensor M3 located at the slat gap. The distinctive characteristics of the broadband hump at $St_1$ and the slat tone at $St_2$, as well as the different characteristics between the three configurations were demonstrated by phase-space analysis of the wavelet coefficients. The power spectral density of the wavelet coefficients at the frequencies of interest pointed out the modulation frequency to be the vortex shedding frequency ($St_2$). Additionally, the statistical analysis of the wavelet coefficients indicated that the $St_1$ was of different nature and the source of the broadband hump to be located at M3 close to the slat gap. The results from the wavelet analysis showed the intermittent nature of the slat tones hidden behind the seemingly deterministic

resonances. The wavelet coefficients from various remote sensors were subject to DMD analysis, which highlighted the difference between the nature of $St_1$ and $St_2$. Furthermore, the slat based Strouhal numbers were segregated into two windows and were subject to mrDMD analysis, which revealed the modulation frequency of the $St_1$ and $St_2$. The application of these techniques provided the characterization of the dynamics of the slat tones. Overall, this study demonstrates that the $St_1$ and $St_2$ tones are relatively different in nature and that $St_1$ is not solely generated due to Rossiter cavity modes, concurring with the previous hypothesis. The source of the $St_1$ was identified to be at the slat gap at location M3 possibly due to the high-velocity flow passing through it. The identified slat noise nature could lead to improved noise reduction mechanism and the new comprehensive data-base within the slat cove region provides a reference for future experimental and numerical studies.

## ACKNOWLEDGEMENT

The high-lift device used in this study was manufactured as part of a completed project sponsored by Embraer.

## DATA AVAILABILITY

The data that support the findings of this study are available from the corresponding author upon reasonable request.

## REFERENCES

[1]M. Szőke, D. Fiscaletti, and M. Azarpeyvand, "Uniform flow injection into a turbulent boundary layer for trailing edge noise reduction," Physics of Fluids **32**, 085104 (2020).

[2]M. Szőke, D. Fiscaletti, and M. Azarpeyvand, "Effect of inclined transverse jets on trailing-edge noise generation," Physics of Fluids **30**, 085110 (2018).

[3]H. Kamliya Jawahar, R. Theunissen, M. Azarpeyvand, and C. R. I. da Silva, "Flow characteristics of slat cove fillers," Aerospace Science and Technology **100**, 105789 (2020).

[4]H. Kamliya Jawahar, S. A. Showkat Ali, M. Azarpeyvand, and C. R. I. da Silva, "Aerodynamic and aeroacoustic performance of high-lift airfoil fitted with slat cove fillers," Journal of Sound and Vibration **479**, 115347 (2020).

[5]H. Kamliya Jawahar, M. Azarpeyvand, R. Theunissen, and C. R. I. da Silva, "Aerodynamic and aeroacoustic performance of three-element high lift airfoil fitted with various cove fillers," in *2018 AIAA/CEAS Aeroacoustics Conference* (2018).

[6]H. Kamliya Jawahar, S. A. Showkat Ali, M. Azarpeyvand, and R. I. Carlos, "Aeroacoustic performance of threeelement high lift airfoil with slat cove fillers," in *25th AIAA/CEAS Aeroacoustic conference* (2019).

[7]H. Kamliya Jawahar, M. Azarpeyvand, and C. Silva, "Numerical investigation of high-lift airfoil fitted with slat cove filler," in *25th AIAA/CEAS Aeroacoustics Conference* (2019) p. 2439.

[8]H. Kamliya Jawahar, M. Azarpeyvand, and C. Ilario, "Experimental investigation of flow around three-element high-lift airfoil with morphing fillers," in *23rd AIAA/CEAS Aeroacoustics Conference* (2017) p. 3364.

[9]H. Kamliya Jawahar, Q. Ai, and M. Azarpeyvand, "Experimental and numerical investigation of aerodynamic performance for airfoils with morphed trailing edges," Renewable Energy **127**, 355–367 (2018).

[10]S. A. Showkat Ali, M. Azarpeyvand, and C. R. I. da Silva, "Trailing-edge flow and noise control using porous treatments," Journal of Fluid Mechanics **850**, 83–119 (2018).

[11]S. A. Showkat Ali, M. Azarpeyvand, and C. R. I. da Silva, "Trailing edge bluntness noise reduction using porous treatments," Journal of Sound and Vibration **474**, 115257 (2020).

[12]S. A. Showkat Ali, M. Azarpeyvand, M. Szőke, and C. R. Ilário da Silva, "Boundary layer flow interaction with a permeable wall," Physics of Fluids **30**, 085111 (2018).

[13]A. Afshari, M. Azarpeyvand, A. A. Dehghan, M. Szoke, and R. Maryami, "Trailing-edge flow manipulation using streamwise finlets," Journal of Fluid Mechanics **870**, 617–650 (2019).

[14]X. Liu, H. Kamliya Jawahar, M. Azarpeyvand, and R. Theunissen, "Aerodynamic performance and wake development of airfoils with serrated trailing-edges," AIAA Journal **55**, 3669–3680 (2017).

[15]Y. D. Mayer, B. Lyu, H. K. Jawahar, and M. Azarpeyvand, "A semi-analytical noise prediction model for airfoils with serrated trailing edges," Renewable Energy **143**, 679–691 (2019).

[16]S. S. Vemuri, X. Liu, B. Zang, and M. Azarpeyvand, "On the use of leading-edge serrations for noise control in a tandem airfoil configuration," Physics of Fluids **32**, 077102 (2020).

[17]H. Kamliya Jawahar, S. A. Showkat Ali, and M. Azarpeyvand, "Serrated slat cusp for high-lift device noise reduction," Physics of Fluids **33**, 015107 (2021).

[18]S. Olson, F. Thomas, and R. Nelson, "Mechanisms of slat noise production in a 2d multi-element airfoil configuration," in *7th AIAA/CEAS Aeroacoustics Conference and Exhibit* (2001) p. 2156.

[19]M. R. Khorrami, "Understanding slat noise sources," in *Colloquium EUROMECH*, Vol. 449 (Citeseer, 2003) pp. 9–12.

[20]A. Kolb, P. Faulhaber, R. Drobietz, and M. Grünewald, "Aeroacoustic wind tunnel measurements on a 2d high-lift configuration," in *13th AIAA/CEAS Aeroacoustics Conference* (2007) p. 3447.

[21]J. Mendoza, T. Brooks, and W. Humphreys Jr, "An aeroacoustic study of a leading edge slat configuration," International Journal of Aeroacoustics **1**, 241–274 (2002).

[22]S. Hein, T. Hohage, W. Koch, and J. Schöberl, "Acoustic resonances in a high-lift configuration," Journal of Fluid Mechanics **582**, 179–202 (2007).

[23]M. Murayama, K. Nakakita, K. Yamamoto, H. Ura, Y. Ito, and M. M. Choudhari, "Experimental study on slat noise from 30p30n three-element high-lift airfoil at jaxa hard-wall lowspeed wind tunnel," in *20th AIAA/CEAS Aeroacoustics Conference* (2014) p. 2080.

[24]M. Terracol, E. Manoha, and B. Lemoine, "Investigation of the unsteady flow and noise generation in a slat cove," AIAA Journal **54**, 469–489 (2016).

[25]M. M. Choudhari and D. P. Lockard, "Assessment of slat noise predictions for 30p30n high-lift configuration from banc-iii workshop," in *21st AIAA/CEAS aeroacoustics conference* (2015) p. 2844.

[26]C. C. Pagani Jr, D. S. Souza, and M. A. Medeiros, "Slat noise: aeroacoustic beamforming in closed-section wind tunnel with numerical comparison," AIAA Journal **54**, 2100–2115 (2016).

[27]C. C. Pagani, D. S. Souza, and M. A. Medeiros, "Experimental investigation on the effect of slat geometrical configurations on aerodynamic noise," Journal of Sound and Vibration **394**, 256–279 (2017).

[28]K. A. Pascioni and L. N. Cattafesta, "An aeroacoustic study of a leading-edge slat: Beamforming and far field estimation using near field quantities," Journal of Sound and Vibration **429**, 224–244 (2018).

[29]K. A. Pascioni and L. N. Cattafesta, "Unsteady characteristics of a slat-cove flow field," Physical Review Fluids **3**, 034607 (2018).

[30]L. Li, P. Liu, H. Guo, Y. Hou, X. Geng, and J. Wang, "Aeroacoustic measurement of 30p30n high-lift configuration in the test section with kevlar cloth and perforated plate," Aerospace Science and Technology **70**, 590–599 (2017).

[31]L. Li, P. Liu, H. Guo, X. Geng, Y. Hou, and J. Wang, "Aerodynamic and aeroacoustic experimental investigation of 30p30n high-lift configuration," Applied Acoustics **132**, 43–48 (2018).

[32]L. Li, P. Liu, Y. Xing, and H. Guo, "Time-frequency analysis of acoustic signals from a high-lift configuration with two wavelet functions," Applied Acoustics **129**, 155–160 (2018).

[33]L. Li, P. Liu, Y. Xing, and H. Guo, "Wavelet analysis of the far-field sound pressure signals generated from a high-lift configuration," AIAA Journal **56**, 432–437 (2018).

[34]W. Horne, K. James, T. Arledge, P. Soderman, N. Burnside, and S. Jaeger, "Measurements of 26%-scale 777 airframe noise in the nasa ames 40-by 80 foot wind tunnel," in *11th AIAA/CEAS Aeroacoustics Conference* (2005) p. 2810.

[35]C. Streett, J. Casper, D. Lockard, M. Khorrami, R. Stoker, R. Elkoby, W. Wenneman, J. Underbrink, W. Wenneman, and J. Underbrink, "Aerodynamic noise reduction for high-lift devices on a swept wing model," in *44th AIAA Aerospace Sciences Meeting and Exhibit* (2006) p. 212.

[36]C. Andreou, W. Graham, and H.-C. Shin, "Aeroacoustic study of airfoil leading edge high-lift devices," in *12th AIAA/CEAS Aeroacoustics Conference* (2006) p. 2515.

[37]C. Andreou, W. Graham, and H.-C. Shin, "Aeroacoustic comparison of airfoil leading edge high-lift geometries and supports," in *45th AIAA Aerospace Sciences Meeting and Exhibit* (2007) p. 230.

[38]T. Imamura, H. Ura, Y. Yokokawa, S. Enomoto, K. Yamamoto, and T. Hirai, "Designing of slat cove filler as a noise reduction device for leading-edge slat," in *13th AIAA/CEAS Aeroacoustics Conference* (2007) p. 3473.

[39]H. Ura, Y. Yokokawa, T. Imamura, T. Ito, and K. Yamamoto, "Investigation of airframe noise from high lift configuration model," in *46th AIAA Aerospace Sciences Meeting and Exhibit* (2008) p. 19.

[40]A. Shmilovich, Y. Yadlin, and D. M. Pitera, "Wing leading edge concepts for noise reduction," in *27th International Congress of the Aeronautical Sciences* (2010).

[41]A. Shmilovich, Y. Yadlin, *et al.*, "High-lift systems for enhanced takeoff performance," in *28th International Congress of the Aeronautical Sciences* (2012).

[42]W. D. Scholten, D. J. Hartl, T. L. Turner, and R. T. Kidd, "Development and analysis-driven optimization of superelastic slat-cove fillers for airframe noise reduction," AIAA Journal **54**, 1078–1094 (2016).

[43]J. Tao and G. Sun, "A novel optimization method for maintaining aerodynamic performances in noise reduction design," Aerospace Science and Technology **43**, 415–422 (2015).

[44]Y. Zhang, A. O'Neill, L. N. Cattafesta, K. Pascioni, M. Choudhari, M. R. Khorrami, D. P. Lockard, and T. Turner, "Assessment of noise reduction concepts for leading-edge slat noise," in *2018 AIAA/CEAS Aeroacoustics Conference* (2018) p. 3461.

[45]Y. D. Mayer, H. K. Jawahar, M. Szőke, S. A. S. Ali, and M. Azarpeyvand, "Design and performance of an aeroacoustic wind tunnel facility at the university of bristol," Applied Acoustics **155**, 358–370 (2019).

[46]E. Manoha and M. Pott-Pollenske, "Leisa2: an experimental database for the validation of numerical predictions of slat unsteady flow and noise," in *21st AIAA/CEAS Aeroacoustics Conference* (2015) p. 3137.

[47]A. Garcia-Sagrado and T. Hynes, "Wall pressure sources near an airfoil trailing edge under turbulent boundary layers," Journal of Fluids and Structures **30**, 3–34 (2012).

[48]X. Liu, *Aerodynamic and wake development of aerofoils with trailing-edge serrations*, Ph.D. thesis, University of Bristol (2018).

[49]H. Kamliya Jawahar, *Aerodynamic and aeroacoustic performance of morphing structures*, Ph.D. thesis, University of Bristol (2019).

[50]J. N. Kutz, S. L. Brunton, B. W. Brunton, and J. L. Proctor, *Dynamic mode decomposition: data-driven modeling of complex systems* (SIAM, 2016).

[51]S. L. Brunton and J. N. Kutz, *Data-driven science and engineering: Machine learning, dynamical systems, and control* (Cambridge University Press, 2019).

[52]B. W. Brunton, L. A. Johnson, J. G. Ojemann, and J. N. Kutz, "Extracting spatial–temporal coherent patterns in large-scale neural recordings using dynamic mode decomposition," Journal of Neuroscience Methods **258**, 1–15 (2016).

[53]J. H. Tu, C. W. Rowley, D. M. Luchtenburg, S. L. Brunton, and J. N. Kutz, "On dynamic mode decomposition: Theory and applications," Journal of Computational Dynamics **1**, 291–421

(2014).

[54]J. Rossiter, "Wind tunnel experiments on the flow over rectangular cavities at subsonic and transonic speeds," RAE Technical Report No. 64037 (1964).

[55]J. Morlet, "Sampling theory and wave propagation," in *Issues in acoustic Signal-image processing and recognition* (Springer, 1983) pp. 233–261.

[56]M. Farge, "Wavelet transforms and their applications to turbulence," Annual Review of Fluid Mechanics **24**, 395–458 (1992).

[57]H. Kamliya Jawahar, M. Azarpeyvand, and C. R. I. da Silva, "Acoustic and flow characteristics of an airfoil fitted with morphed trailing edges," Experimental Thermal and Fluid Science , 110287 (2020).

[58]P. S. Addison, *The illustrated wavelet transform handbook: introductory theory and applications in science, engineering, medicine and finance* (CRC press, 2017).

[59]T. Sayadi, P. J. Schmid, F. Richecoeur, and D. Durox, "Parametrized data-driven decomposition for bifurcation analysis, with application to thermo-acoustically unstable systems," Physics of Fluids **27**, 037102 (2015).

[60]S. T. Dawson, M. S. Hemati, M. O. Williams, and C. W. Rowley, "Characterizing and correcting for the effect of sensor noise in the dynamic mode decomposition," Experiments in Fluids **57**, 42 (2016).

[61]Z. Bai, E. Kaiser, J. L. Proctor, J. N. Kutz, and S. L. Brunton, "Dynamic mode decomposition for compressive system identification," AIAA Journal **58**, 561–574 (2020).